Front. Med. 2025, 19(6): 1214−1235
https://doi.org/10.1007/s11684-025-1176-9

RESEARCH ARTICLE

Metabolic biomarkers for predicting onset and severity of CAR-T therapy-induced cytokine release syndrome in multiple myeloma

Xiaolin Ma[1,2,*], Tuantuan Gui[1,2,*], Shuangshuang Yang[1,*], Shiwei Jin[1,*], Jing Qiao[1], Yinyin Xie[1], Junyu Wang[1,3], Wanyan Ouyang[1], Gaoxian Song[1], Xiao Yi[1,2], Chenglin Liu[1], Mengmeng Pan[1], Weiyang Liu[1], Niu Qiao[1], Yuting Dai[1], Yi Tao[1], Jie Xu[1], Tong Yin[1], Hai Fang[1], Jianqing Mi[1,4], Sai-Juan Chen (✉)[1]

[1]Shanghai Institute of Hematology, State Key Laboratory of Medical Genomics, National Research Centre for Translational Medicine at Shanghai, Research Unit of Hematologic Malignancies Genomics and Translational Research of Chinese Academy of Medical Sciences, Ruijin Hospital Affiliated to Shanghai Jiao Tong University School of Medicine, Shanghai 200025, China; [2]School of Life Sciences and Biotechnology, Shanghai Jiao Tong University, Shanghai 200030, China; [3]Department of Medical Oncology, Fudan University Shanghai Cancer Center, Shanghai 200032, China; [4]Shanghai Key Laboratory of Gene Editing and Cell-based Immunotherapy for Hematological Diseases, Shanghai 200025, China

Abstract **Chimeric antigen receptor T-cell (CAR-T) therapy has been successfully applied in clinical treatment, especially for hematologic malignancies such as multiple myeloma (MM), but its broad application is limited by cytokine release syndrome (CRS), a potentially life-threatening complication. Although metabolic alterations are known to accompany CRS, predictive biomarkers for its onset, severity, and associated metabolic remodeling remain unknown, hindering proactive clinical management. Here, we analyzed longitudinal serum metabolic profiles from 19 patients with relapsed/refractory MM receiving CAR-T therapy, with validation in an independent cohort of 23 patients. We observed dysregulated arginine metabolism that progressed alongside clinical CRS. At pre-lymphodepletion (Day −5), over half of differentially abundant metabolites were enriched in unsaturated fatty acid (UFA) synthesis pathways, which were exclusively upregulated in patients who later developed severe CRS. Furthermore, two lysophosphatidylcholines, namely, lysoPC(16:0) and lysoPC(15:0), were significantly associated with delayed CRS onset, with elevated concentrations correlated with a prolonged time to onset; this association was independently validated. These findings revealed that arginine metabolism was a pathological axis in CRS, UFAs were severity predictors, and specific lysoPCs were modulators of onset time. Collectively, they provide proactive CRS management, addressing critical gaps in predictive biomarkers to advance the safe, broad CAR-T application in MM.**

Keywords multiple myeloma (MM); chimeric antigen receptor T-cell (CAR-T) therapy; cytokine release syndrome (CRS); longitudinal metabolomics; metabolic biomarkers; early prediction

Introduction

Multiple myeloma (MM) ranks as the third most common hematologic malignancy [1], characterized by its gradual onset, persistent progression, and high relapse rates [2]. Although advancements in therapy such as proteasome inhibitors, immunomodulators, and monoclonal antibodies have improved patient outcomes, most patients with MM remain incurable. This is particularly true for relapsed/refractory MM (R/R MM), which is often resistant to conventional treatments [3,4]. This unmet clinical need urgently requires the development of novel strategies to overcome drug resistance and achieve sustained remission.

In recent years, chimeric antigen receptor T cell (CAR-T) therapy has emerged as a breakthrough treatment for patients with R/R MM. By modifying patients' autologous T cells to target tumor-specific antigens, CAR-T therapy activates the adaptive immune system and induces remarkable tumor clearance [5]. Clinical

Received August 1, 2025; accepted August 21, 2025

Correspondence: Sai-Juan Chen, sjchen@stn.sh.cn

*These authors made equal contributions to the paper.

trials have demonstrated that CAR-T therapy improves complete remission (CR) rates and achieves durable minimal residual disease negativity [5]. However, its broad clinical application is limited by severe toxic reactions, most notably cytokine release syndrome (CRS). With an incidence ranging from 35% to 93% (median 77%) [6], CRS is a major obstacle to widespread implementation.

CRS is a systemic inflammatory response triggered by the overactivation of CAR-T cells, characterized by a surge in pro-inflammatory cytokine release (e.g., IL-6, IFN-γ, and TNF-α) [7,8]. Clinical symptoms range from self-limited fever to critical multi-organ failure, with severity influenced by factors such as the dose of CAR-T cell infusion, tumor load, host inflammatory status, and comorbidities [9]. Although key aspects of the pathophysiological mechanisms of CRS are understood, the intricate and dynamic immunometabolic regulatory networks underlying its development and progression remain poorly defined.

To address this gap, researchers must resolve the interplay between host metabolism and immune dysregulation during CRS. Serum metabolomics provide a powerful tool for this purpose; it captures systemic metabolic reprogramming triggered by CAR-T activation in real time by analyzing dynamic changes in blood small-molecule metabolites [10]. Longitudinal metabolomics can detect metabolic warning signals before CRS onset. Tracking time-series fluctuations in metabolite levels following infusion facilitates the identification of early predictive markers, elucidates pathogenic pathways, and reveals potential therapeutic targets. Ultimately, our findings may optimize CRS risk stratification, guide clinical intervention strategies, and enhance the safety of CAR-T therapy.

In this study, we employed longitudinal serum metabolomics in patients with R/R MM undergoing CAR-T therapy. We identified early predictive biomarkers for CRS onset (specifically dysregulated arginine metabolism) and pre-lymphodepletion metabolic signatures (involving unsaturated fatty acids (UFAs) and tryptophan pathways) that predict CRS severity. Furthermore, we validated key biomarkers and demonstrated their association with immune cell activation dynamics, highlighting pathways for proactive intervention to enhance CAR-T therapeutic safety.

Materials and methods

Blood collection and sample preparation

Nineteen patients with R/R MM treated with ciltacabtagene autoleucel (cilta-cel, with an overall response rate (ORR) of 89.6% [11], complete remission (CR) rate of 77.1% [11], and 5-year overall survival (OS) rate of 49.1% [12]) were enrolled in the study: 11 from the previously reported Legend-2 phase I trial (ChiCTR-ONH-17012285) [13] and 8 from the CARTFAN-1 phase II trial (NCT03758417) [11]. The methods for product transfusion and lymphodepletion prior to transfusion followed previously reported protocols [11,13]. In total, 152 patient serum samples (over 4 weeks) and 20 age/sex-matched healthy control (HC) samples were collected, whereas serum samples from an additional 23 patients were collected as an independent validation cohort (NCT05759793; ChiCTR1900028573; CRT20181007; CXSL1900060).

Peripheral blood was drawn from the upper forearms of participants who had fasted overnight at nine time points: 5 days before CAR-T cell infusion, baseline (the day of CAR-T cell infusion but before infusion), 3–5 days, 6–9 days, 10–12 days, 13–15 days, 20–22 days, 28–32 days, and the first follow-up to achieve CR. Samples were placed on ice immediately after collection to prevent deterioration and processed together immediately after the final sample was collected. Serum samples were then collected and aliquoted for freezing. Serum was collected in yellow vacuum blood collection tubes and centrifuged at 3000 rpm for 20 min at room temperature. All peripheral blood samples were characterized using multiple omics methods, including analysis of peripheral blood mononuclear cells (PBMCs) for RNA sequencing and serum for untargeted and targeted metabolomics and cytokine assays. Patient clinical response was evaluated according to the International Myeloma Working Group consensus response criteria [13,14].

Untargeted metabolomics from serum by liquid chromatography–mass spectrometry

All pre-treated samples were analyzed for untargeted metabolomics using a previously described method [15]. Initially, proteins were precipitated in 150 μL of methanol/acetonitrile (v:v = 1:1) solution, followed by centrifugation at 15 000 *g* for 10 min at 4 °C to collect the supernatant containing the extracted metabolites. The metabolite samples underwent an additional centrifugation step before analysis.

Untargeted analysis was conducted using a UHPLC LC-30A system (Shimadzu) connected to a Sciex Triple Q-TOF 6600 plus system (Sciex). Chromatographic separations were carried out on a Waters Acquity HSS T3 column (100 mm × 2.1 mm, 1.8 μm) in positive and negative ion modes. Gradient elution was performed with mobile phase A (water containing 0.1% formic acid, v/v) and mobile phase B (acetonitrile containing 0.1% formic acid). The gradient elution program started at 1% B for 1.5 min, increased linearly to 99% B by 13 min, and was maintained for 3.5 min. It then returned to 1% B in

0.1 min and was maintained for 3.4 min for post-equilibration. The flow rate was set at 0.3 mL/min, and the column temperature was maintained at 40 °C. During data collection, the autosampler temperature was set at 8 °C, with an injection volume of 2 μL.

The following parameters were used for the Triple TOF 6600 plus mass spectrometer. For the positive ion mode, a spray voltage of 5.5 kV was applied. For the negative ion mode, a spray voltage of −4.5 kV was used. The source temperature was maintained at 550 °C. The pressures for the curtain gas, gas 1, and gas 2 were set to 40, 55 and 55 psi, respectively.

Automated MS2 scans were performed using information-dependent acquisition, targeting the 10 most intense metabolite ions in each full scan cycle. The mass-to-charge ratio (m/z) scan ranges were set to 60–1000 Da for precursor ions and 50–1000 Da for product ions. The collision energy was set to 35 V for positive ion mode and −35 V for negative ion mode, with a collision energy spread of 15 V.

Metabolomic data analysis

We employed a three-step approach for metabolite identification. Initially, we utilized the Sciex commercial in-house metabolite library, identifying compounds based on precise mass ratio (m/z) and MS/MS spectral data, with a mass tolerance of 10 ppm and a minimum MS/MS spectral match score of 0.8. Additional metabolites were identified using accurate mass, isotopic patterns, and MS/MS spectra from public databases via the R software package "metID" [16]. Preference was given to compounds with high m/z matching scores (with library score ⩾ 50). Finally, metabolic peaks not matched in public databases were analyzed using MetDNA.

To handle missing values, we imputed them with 1/10 of the minimum value of the corresponding variable. Data from positive and negative modes were merged. Batch effects were then corrected using the systematic error removal in random forests (SERRF) method, which minimized their influence on the bulk metabolomics data using quality control (QC) samples [17]. QC samples were excluded from further analysis if their relative standard deviation was > 0.3. Principal component analysis (PCA) was conducted to examine the overall distribution of the sample data and assess data quality. After applying the SERRF method, the serum metabolic profiles no longer showed clustering based on the sampling batch, as illustrated in Fig. S1.

Differential metabolite calculations and pathway enrichment analysis

Processed matrices were extracted and analyzed using the limma R package (version 3.58.1) to identify significantly altered metabolic profiles and compounds [18]. Metabolites exhibiting an absolute fold change > 1.5 or < 0.667 and an adjusted $P < 0.05$ were classified as significantly different. We conducted enrichment analysis and metabolic pathway analysis on these metabolite sets using MNet R package (version 0.1.0) to identify pathways with relative enrichment ($P < 0.1$). A higher enrichment ratio indicates a greater degree of enrichment.

Differential abundance analysis of metabolic pathways

To characterize metabolic pathway dysregulation, we employed differential abundance (DA) analysis [19] based on the KEGG Compound Database. This approach calculates DA scores using the formula:

$$\mathrm{DA} = \frac{(\text{number of metabolites increased} - \text{number of metabolites decreased})}{\text{number of metabolites measured in the pathway}}$$

The DA scores range from −1 to 1, where a score of −1 indicates a complete decrease in the abundance of all metabolites in a pathway, and a score of 1 indicates a complete increase. Pathways included in the calculations contained at least two measured metabolites with a fold change of 1.5 or more, and $P < 0.05$ was used as the screening criterion.

Soft clustering method

The soft clustering approach was executed using the fuzzy c-means algorithm available in the Mfuzz R package (v2.62.0). This method aimed to iteratively assign genes to various clusters based on their expression profiles [20]. Following normalization, metabolites were allocated to specific clusters according to their membership scores (α).

Analyzing metabolites on a supra-hexagonal map

To visualize the metabolite–sample matrix, we employed the self-organizing learning algorithm available in the supraHex package [21] to generate a supra-hexagonal map that displays 2D images of samples and metabolites. Each small hexagonal cell on the map represents a cluster of metabolites exhibiting similar patterns across samples, with color shading reflecting metabolite levels.

Correlation analysis between multi-omics

Correlations were calculated using the corrplot R package (0.92). Significant correlations were defined as those with coefficient $|r| > 0.2$ and adjusted $P < 0.05$.

Multivariate analysis of metabolites associated with CAR-T efficacy and one-year relapse

To evaluate the combined influence of 422 metabolites on

CAR-T therapy efficacy and one-year relapse risk, we defined therapeutic response as a binary outcome based on assessments at discharge post-infusion: patients achieving ⩾ very good partial response (VGPR) constituted the good-efficacy group, whereas those with responses inferior to VGPR comprised the poor-efficacy group. Metabolite features significantly associated with clinical outcomes were selected using a VIP threshold > 1.0, with robustness assessed through 10-fold cross-validation coupled with 100 permutations to mitigate overfitting. Multivariate analyses involved three approaches: (1) conditional logistic regression with lasso penalization ("Lasso"), (2) conditional logistic regression with elastic net penalization ("Elastic Net"), and (3) random forests. Lasso and elastic net regressions were performed using the MNet R package (0.1.0); ridge and lasso regressions were conducted using the glmnet R package; and random forest analysis utilized the Bournta R package (8.0.0).

Determination of arginine synthesis via targeted liquid chromatography–mass spectrometry

Arginine synthesis (AS) was analyzed using liquid chromatography–mass spectrometry/mass spectrometry (LC–MS/MS). Serum samples were thawed at room temperature and added with 200 μL of methanol. The mixture was vortexed for 3 min and then centrifuged at 4 °C for 5 min at 12 000 rpm. Subsequently, 100 μL of the supernatant was subjected to LC–MS/MS analysis. AS metabolites were analyzed using a Sciex 6500 triple quadrupole mass spectrometer (Sciex, Framingham, MA, USA). The mass spectrometer parameters were optimized, and the samples were analyzed automatically using a multiple reaction monitoring approach. AS concentrations were quantified using calibration curves specific to each metabolite in this pathway.

Statistics and reproducibility

Frequency tables and summary statistics were employed to describe data distributions. For omics data analyses, the Mann–Whitney Wilcoxon test was used to compare continuous variables, while Pearson's chi-square test and Fisher's exact test were used for categorical variables, unless specified otherwise. Survival curves were generated using the Kaplan–Meier method and compared using the Log-rank test. *P*-values were adjusted for the false discovery rate using the Benjamini–Hochberg method. Statistical analyses were conducted using R version 4.3.2 or GraphPad Prism version 8.0.2. Statistical significance thresholds were defined as follows: ****$P < 0.0001$, ***$P < 0.001$, **$P < 0.01$, *$P < 0.05$.

Results

Cohort characteristics and longitudinal study design

This study enrolled 19 patients with R/R MM treated with cilta-cel, a B cell maturation antigen, targeting CAR-T therapy. The cohort comprised 11 participants from the Phase I Legend-2 trial, as previously reported [13], and 8 from the Phase II CARTFAN-1 trial (Fig. 1A) [11]. We collected 152 serum samples from these 19 patients with R/R MM (ages 35–68 years; 63.16% male and 36.84% female) and 20 samples from age- and sex-matched HCs for reference (ages 46–70 years, $P = 0.3$; 85% male and 15% female, $P = 0.535$). An independent cohort of 23 patients was also studied for validation (Fig. 1B). This comparative design helped to confirm that the reported changes were induced by CAR-T cell infusion.

Table 1 summarizes the baseline demographics characteristics of the discovery cohort ($N = 19$) and HCs ($N = 20$), and Table 2 compares these characteristics between the severe and mild CRS groups (Tables 1, 2, and S1). Comorbidity information is additionally documented in these tables, as certain conditions may influence metabolic outcomes [22]. Although our exclusion criteria mitigate confounding effects from acute organ dysfunction and severe systemic illnesses on metabolomic analyses, mild-to-moderate comorbidities remain present in enrolled patients and may affect metabolomic profiles. The majority of participants experienced CRS, the most common complication of CAR-T therapy for MM. Clinical characteristics associated with CRS severity were analyzed in a previous work, adopting criteria defined by the CARTOX working group for grading CRS [13]. In our study, CRS grade 3 or higher were classified as severe adverse effects, and grades 1 and 2 were classified as mild adverse effects. Patients were grouped based on their highest CRS grade (Fig. 1A and Table S2). No significant differences were observed between the severe and mild groups in terms of sex, age, BMI, serum M protein level, or other baseline characteristics (Table 2). Unfortunately, three patients in the severe group (CZ03, RJ30, and RJ31) died early due to severe CRS (CRS grade 5), whereas seven patients remain in ongoing remission (Fig. 1A).

To gain insights into CRS development, we collected intravenous blood specimens at baseline (Day 0, pre-infusion) and on 3–5 (Days 3–5), 6–9 (Days 6–9), 10–12 (Days 10–12), 13–15 (Days 13–15), 20–22 (Days 20–22), and 28–32 days (Days 28–32) after CAR-T infusion. The inflammatory reaction was divided into seven phases over 30 days: baseline (Day 0, pre-infusion), latent (Days 3–5), fever (Days 6–9), acute aggravation (Days 10–12 and Days 13–15), resolving (Days 20–22), and remission (Days 28–32) periods (Fig. 1B). In addition, the discovery

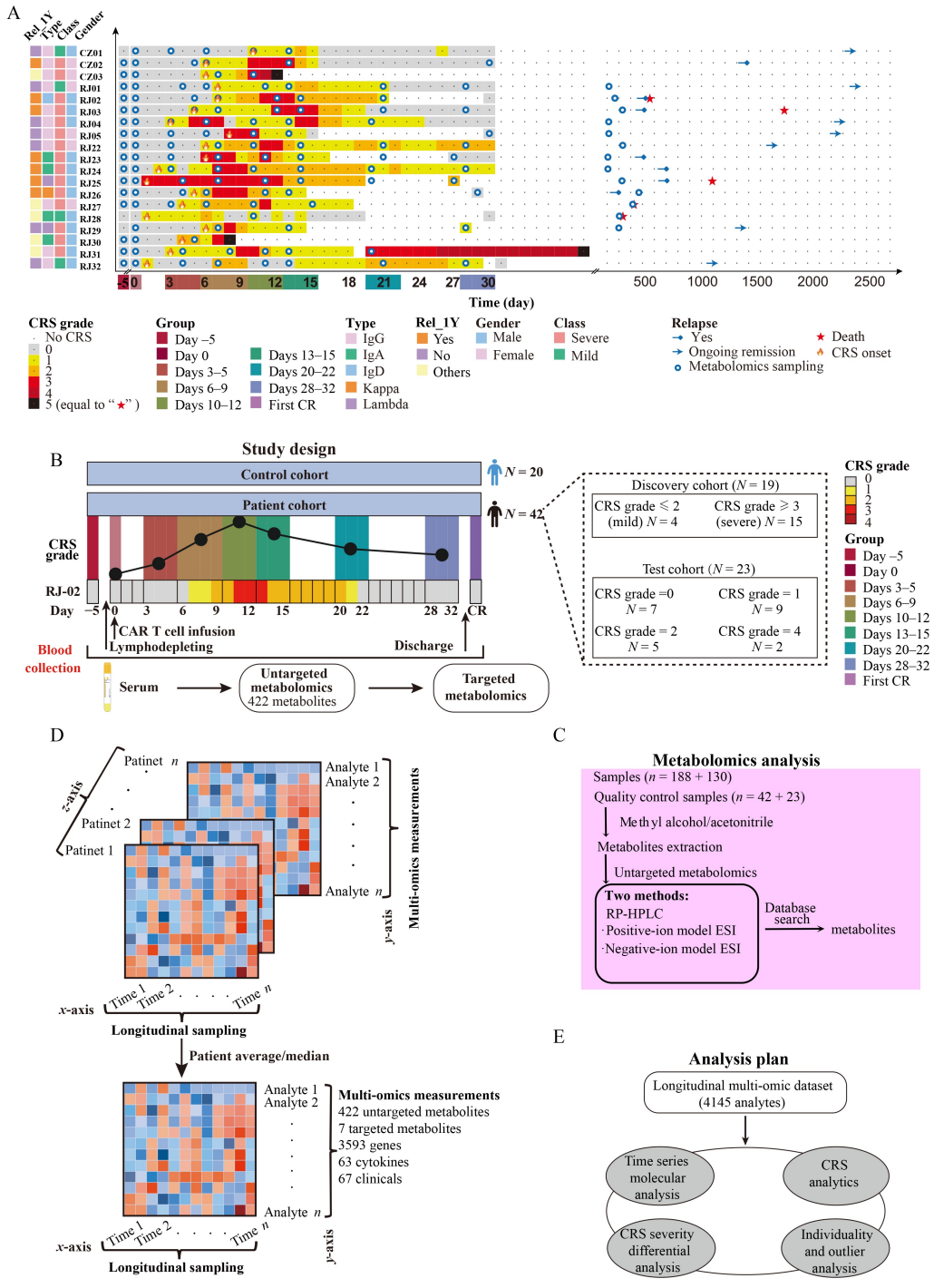

Fig. 1 Overview of the study cohort and design. (A) Timeline of the discovery cohort: The *y*-axis shows patient IDs, and the *x*-axis displays days after CAR-T therapy. The cohort includes 19 patients (13 males and 6 females), with key clinical characteristics (e.g., CRS class and relapse status) summarized in the right panel. Rel_1Y defined as the relapse status within one year. Stars indicate death patients. Blue dots mark metabolomics sampling time points. (B) Metabolomic analysis was performed on 301 serum samples collected from 42 patients with R/R MM (19 patients from the discovery cohort and 23 from the validation cohort), along with 20 serum samples from 20 control individuals (single time point). These serum samples were collected at nine time points spanning the therapeutic course: before lymphodepletion, prior to cell infusion, at six longitudinal points during the first 4 weeks post-infusion, and at the first documented complete remision (CR) time point during post-discharge follow-up. (C) In total, 318 serum samples and 65 quality control samples were processed using two methods, identifying 422 and 473 metabolites, respectively. (D) Conceptual data structure: the *x*-axis represents sampling time points, the *y*-axis represents analytes from multi-omics data, and the z-axis represents individual patients. (E) Metabolomics analysis plan: (1) time-series analysis of CAR-T therapy-related metabolites, (2) correlation analysis to identify metabolites associated with CRS class and onset, (3) differential metabolite analysis between the severe and mild CRS groups, and (4) individual patient-level.

Table 1 Baseline clinical characteristics (MM versus HC)

Variables	Multiple myeloma ($N = 19$)	Healthy controls ($N = 20$)	P value
Sex, *n* (%)			0.535[a]
Male	12 (63.16)	17 (85)	
Female	7 (36.84)	3 (15)	
Age, year			
Median (range)	57 (35–68)	52 (46–70)	0.300[b]
Serum M protein, g/L			
Median (range)	29.62 (11.3–64.5)		
Ig Type, *n* (%)			
IgG	11 (68.75)		
IgA	4 (25)		
IgD	1 (6.25)		
Light chain type, *n* (%)			
λ	2 (66.67)		
κ	1 (33.3)		
Clonal BM plasma cells, %			
Median (range)	9.95 (0.28–69)		
ALT (10–64), IU/L			
Median (range)	18.5 (11–86)	21 (11–37)	0.770[b]
AST (8–40), IU/L			
Median (range)	23 (12–157)	22.5 (17–30)	0.295[b]
TBIL (4.7–24), μmol/L			
Median (range)	10.5 (6–21.1)	13.15 (5.4–18.9)	0.089[b]
TBA (1–10), μmol/L			
Median (range)	4.35 (1.7–23.8)	2.95 (1.4–7.9)	0.060[b]
BUN (2.5–7.1), mmol/L			
Median (range)	4.5 (1.86–8.8)	5 (3.9–7.1)	0.472[b]
Range	1.86–8.8	3.9–7.1	
CREA (62–115), μmol/L			
Median (range)	71.5 (47–108)	78.5 (55–103)	0.299[b]

[a]P is calculated by χ^2 test. [b]P is calculated by t-test.

cohort (N = 19) provided blood samples before lymphodepletion (Day −5) and at the first CR during follow-up (First CR; Fig. 1B). In-depth multi-omics profiling was conducted on each sample, including serum metabolomics (targeted and untargeted), cytokine profiling (Luminex), clinical characteristics, and metabolic gene expression (RNA-seq) from PBMCs (Fig. S2A). A total of 66 highly frequent clinical laboratory characteristics were selected from the 152 serum samples (Table S3). The metabolomic data set included 422 serum metabolites from the 152 patient samples (collected over 4 weeks) and 20 HC samples (collected at a single time point), quantified via untargeted liquid chromatography–electrospray ionization tandem mass spectrometry (LC–ESI–MS/MS; Fig. 1B and 1C and Tables S4–S6). Targeted metabolomics focused on metabolites involved in the arginine metabolic pathway (Table S9). Data on metabolic-related genes and cytokines were obtained from Yang *et al.* (Tables S7 and S8) [23].

For subsequent analyses, median or average values were calculated across patients within relevant groups (Fig. 1D). After data curation and annotation, the final data set included 4145 analytes (Fig. S2A and Tables S3–S9): 422 untargeted metabolites, 7 targeted metabolites, 3593 genes, 63 cytokines, and 66 clinical laboratory characteristics. The longitudinal multi-omics data set was utilized to (1) characterize the dynamic molecular response to CAR-T therapy; (2) determine molecular associations with CRS and identify predictors of CRS severity; (3) analyze differential responses to CAR-T therapy across CRS grades; and (4) examine the

Table 2 Baseline clinical characteristics (severe vs. mild)

Variables	Mild (CRS grade ⩽ 2) (*N* = 4)	Severe (CRS grade ⩾ 3) (*N* = 15)	*P* value
Sex, *n* (%)			0.865[a]
Male	3 (75)	9 (60)	
Female	1 (25)	6 (40)	
Age, year			
Median (range)	56 (35–61)	58 (40–68)	0.420[b]
BMI (18.5–23.9), kg/m^2			
Median (range)	20.94 (20.37–25.96)	23.46 (18.04–29.06)	0.538[b]
Serum M protein, g/L			
Median (range)	27.4 (11.3–40.2)	31.53 (11.5–64.5)	0.616[b]
Ig Type, *n* (%)			0.719[a]
IgG	3 (75)	8 (66.67)	
IgA	1 (25)	3 (25)	
IgD	0 (0)	1 (8.33)	
Light chain type, *n* (%)			NA[a]
λ	0 (0)	2 (66.67)	
κ	0 (0)	1 (33.33)	
Clonal BM plasma cells, %			
Median (range)	17 (4.5–69)	6 (0.28–45)	0.290[b]
ALT (10–64), IU/L			
Median (range)	21 (13–86)	19 (11–29)	0.049[b]
AST (8–40), IU/L			
Median (range)	16 (12–157)	16 (13–45)	0.259[b]
TBIL (4.7–24), μmol/L			
Median (range)	8.5 (6–15.8)	11.05 (8.1–21.1)	0.347[b]
TBA (1–10), μmol/L			
Median (range)	3.25 (2.8–23.8)	4.8 (1.7–12.5)	0.338[b]
BUN (2.5–7.1), mmol/L			
Median (range)	6.65 (4.1–7.7)	4.35 (1.86–8.8)	0.102[b]
CREA (62–115), μmol/L			
Median (range)	90.5 (47–108)	67.5 (49–101)	0.303[b]

[a]*P* is calculated by χ^2 test. [b]*P* is calculated by *t*-test.

clinical relevance of outlier analyses at the individual level (Fig. 1E).

System-wide multi-omics remodeling induced by CAR-T therapy

The quality of each omics data set was initially examined to ensure the absence of batch effect (Fig. S1). CAR-T therapy induced system-wide changes in 1409 analytes spanning all omics layers (defined as those with at least 1.5-fold change and $P < 0.05$; Fig. 2A and 2B and Tables S10–S12). Samples from the same participant clustered together, indicating consistent intra-individual profiles (Fig. S2B). These changes spanned metabolites, cytokines, and gene expression profiles, reflecting widespread systemic perturbations. Notably, HCs and patients with MMs did not cluster together, even when patients achieved CR status (Fig. S2C).

The group with the most changes, as observed by coefficient of variation (CV), was the acute aggravation phase (Days 10–12 and Days 13–15), in which the arginine biosynthesis and bile acid metabolism pathways were significantly enriched (Fig. S2E and S2F and Tables S13 and S14). We conducted a time-series analysis of serum metabolites across nine time points during CAR-T therapy in patients with MM, identifying 89 unique differentially expressed metabolites (Fig. 2A). The periods of Days 10–12 and Days 13–15 changed most, with 33 and 25 significantly differential metabolites, respectively (Fig. 2B); notably, 44% of these

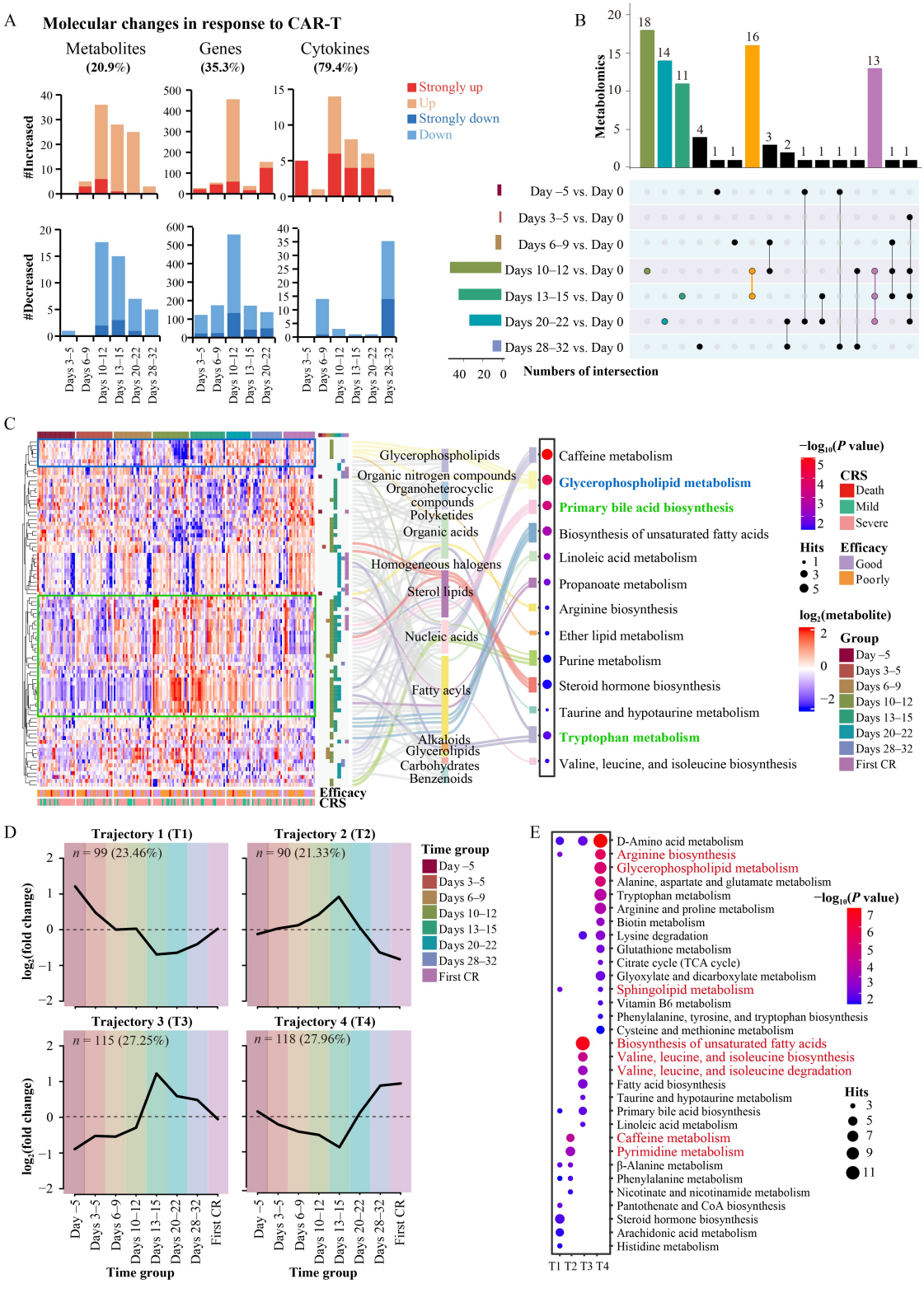

Fig. 2 Molecular response to CAR-T. (A) Multi-omics changes in response to CAR-T therapy. (B) Upset plot of significant metabolites during eight time periods. (C) Heatmap of significant metabolites, the subclass, and the enriched KEGG pathway. Left: heatmap of significant metabolites representing the median $\log_2$(fold change) relative to baseline in the cohort. Metabolites were grouped by clusters. Middle: classification of metabolites. Right: bubble plot showing the enriched KEGG pathway; the size of bubbles represents the number of metabolites enriched in a pathway. (D) Four trajectories of metabolites with different longitudinal trajectories computed with "Mfuzz" analysis (more details in Table S6). (E) Pathway enrichment for the metabolites in four trajectories (more details in Table S17).

metabolites overlapped. DA analysis (calculating DA scores) revealed 18 metabolic pathways significantly affected during Days 10–12 (Fig. S3A and Table S15). Lipid metabolism, especially primary bile acid biosynthesis, exhibited the most substantial changes. Biosynthesis of unsaturated fatty acids (UFAs), tryptophan metabolism, and pyrimidine metabolism also showed high DA scores, and these three pathways changed persistently during the post-CAR-T therapy period. Amino acid metabolism became increasingly dominant, whereas lipid metabolism sustained a high DA score (Fig. S3A–S3C).

Building on these findings, the 89 differentially expressed metabolites revealed distinct metabolic patterns (Fig. 2C). Two metabolite clusters were upregulated at Days 10–12, Days 13–15, and Days 20–22, and they were primarily linked to primary bile acid synthesis, tryptophan metabolism, and propanoate metabolism. Notably, another metabolite cluster (demarcated by the blue rectangle) showed a distinct upregulation at Days 20–22, Days 28–32, and First CR, including seven lysoPC/PE species (key components of glycerophospholipid metabolism), two arachidonic acid (AA) analogs, and one purine derivative. Given their roles as precursors of platelet-activating factors and in platelet remodeling, these metabolites may contribute to platelet remodeling [24], which aligns with the coagulation dysfunction observed post-CRS [24]. These metabolic shifts likely reflect adaptive and recovery processes during the later stages of CAR-T therapy, highlighting the role of lipid metabolism in recovery.

Temporal metabolic trajectories during CAR-T therapy

To investigate dynamic changes in inflammatory responses and metabolic pathways during CAR-T therapy, we utilized high-density sampling. The optimal number of trajectories was determined in the "elbow" plot, with four temporal trajectories identified via the "Mfuzz" method for c-means clustering [20] (Fig. 2D). These trajectories showed distinct patterns of metabolite changes after CAR-T therapy. Some metabolites increased post-CRS and returned to baseline at First CR (Trajectory 3, T3). By contrast, others dropped at Days 13–15, remained low during recovery, and reached their lowest levels at First CR (Trajectory 2, T2). Additional metabolites decreased in response to CAR-T therapy but spiked after the development of CRS (Trajectory 4, T4), or they gradually increased after CRS and returned to baseline at the First CR (Trajectory 1, T1; Fig. 2D and Table S6).

Significant metabolic shifts were observed across these trajectories. Enrichment analysis revealed that arginine biosynthesis and sphingolipid metabolism were enriched in T1 and T4 ($P < 0.01$; Fig. 2E and Table S17), and their member metabolites included L-aspartic acid, L-arginine, N-acetylornithine, L-glutamine, citrulline, and argininosuccinic acid. Low arginine levels have been linked to suppressed CAR-T cell glycolysis and proliferation, as well as poor therapeutic efficacy [25–28]. During the acute aggravation period (Days 10–12), arginine underwent increased catalysis by inducible nitric oxide synthase (iNOS), leading to heightened production of citrulline and nitric oxide (NO), whereas gene expression of arginase (ARG) and glycine amidinotransferase (GATM), a key enzyme of the creatinine pathway, decreased (Fig. 3A). NO acts as an endothelial activator, which increases inflammatory responses [29]. AA levels increased markedly during this time, whereas the expression of the gene encoding nitric oxide synthase 2 (NOS2) was low. Pro-inflammatory substances were also highly secreted [30]. Our RNA-seq data revealed the likely activation of macrophages during this period, consistent with an M1 phenotype (Fig. S3D and S3E and Table S18). Citrulline depletion has been implicated in driving macrophage activation toward the M1 phenotype, with argininosuccinate synthetase 1 (*ASS1*) catalyzing the conversion of citrulline to argininosuccinate [31]. The expression of *ASS1* was dramatically upregulated at Days 6–9, suggesting that citrulline depletion may precede the inflammatory response induced by macrophage activation (Fig. 3A). Phenotypic analysis of immune infiltration of metabolic-related genes revealed macrophage activation, primarily of the M1 type, on Days 6–9 (Fig. S3E). *ASS1* expression varied between mild and severe CRS (Table S18): the mild group showed insignificant changes in *ASS1* upregulation on Day 6–9, whereas the severe group exhibited significant upregulation (Table S18). Macrophages have been implicated in CAR-T-induced CRS release [30], and the notable upregulation of *ASS1* in the severe group may contribute to macrophage activation and subsequent CRS severity [31,32]. These findings collectively highlight the importance of arginine metabolism in immune regulation, macrophage activation, and CRS pathophysiology, suggesting that targeting pathways like *ASS1* modulation could mitigate severe CRS and enhance CAR-T cell therapy efficacy (Tables S19, S20, S35, and S36).

Sphingolipid-related metabolites, such as sphingosine-1-phosphate, showed strong correlation with AA derivatives from the CYP450 pathway (such as 20-HETE, 19S-HETE, and 12R-HET; adjusted $P < 0.05$, $|r| > 0.8$; Table S16). AA is a key regulator of stress responses [5]. "Mfuzz" analysis clustered AA within temporal profile T3 (Table S6), whereas derivatives from its cyclooxygenase (COX) pathway (e.g., 16-phenoxytetra-norprostaglandin E2) and lipoxygenase (LOX) pathway (e.g., leukotriene D4 methyl ester) clustered in T2.

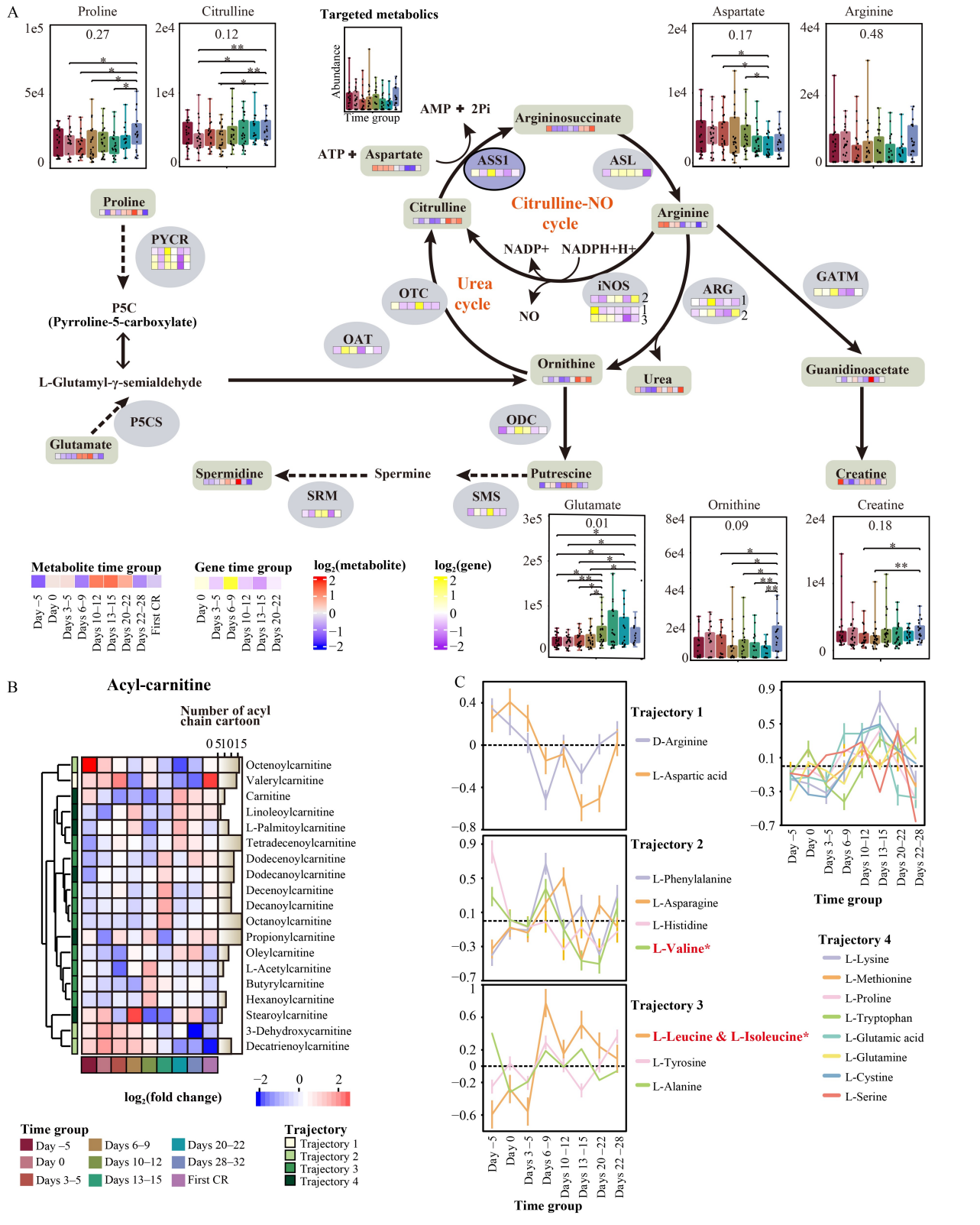

Fig. 3 Metabolites in specific pathways. (A) Targeted analysis of metabolites involved in the arginine metabolic pathway. The boxplots were targeted metabolomic results. The heatmap bar presents the abundance of metabolite and genes. The "purple-white-yellow" represents the gene expression levels, and the "blue-white-red" represents the metabolite abundance. (B) Heatmap of acyl-carnitine and cluster by "Mfuzz". (C) Longitudinal trajectories of significant amino acids in response to CAR-T therapy. The metabolite level is the mean $\log_2$(fold change) relative to baseline, and the bars are the SEM. * means branched chain amino acids.

Similar to T3 metabolites, these derivatives peaked on Days 13–15, indicating that AA activation of the COX and LOX pathways during acute aggravation [6] induced the synthesis of pro-inflammatory mediators. Furthermore, soluble IL-1 receptor II (sIL-1RII), a cytokine that binds IL-1, showed strong associations with cortisol (Fig. S4A and Table S16). Certain AA derivatives (e.g., 16-phenoxytetranorprostaglandin E2) are known to stimulate cortisol secretion, likely limiting excessive inflammation. IL-1 exhibits a robust correlation with the AA metabolic pathway and is involved in key cellular processes via the activation of NF-κB and AP-1 [33].

Pyrimidine and caffeine metabolism were enriched in T2 (adjusted $P < 0.05$; Fig. 2E and Table S17). Pyrimidines support DNA synthesis [34] and T cell activation [35]. Caffeine act as an adenosine receptor antagonist, enhancing immune responses by activating $CD8^+$ T cells, suppressing tumor angiogenesis, and inducing apoptosis [36–38]. Metabolites in these pathways are correlated with cytokines (clinical characteristics) such as IL-1Ra and TNF-RII (Fig. S4B and Table S16), emphasizing their role in metabolic and immune crosstalk [38,39]. Cystatin C (CysC) has anti-inflammatory properties, inhibiting IL-1β and TNF-α release but preserving IL-6 expression [36], thereby indicating the targeted regulation of inflammatory responses. During Days 13–15, the suppression of IL-1 and TNF coincided with increased ribulose and xylose levels, linking metabolic changes to inflammation [37]. Pyrimidine damage products, such as cytosine, are generated during inflammation [40], which may help explain the connection between chronic inflammation and cancer.

The biosynthesis of UFAs and branched-chain amino acids (BCAAs) was elevated in T3, which was associated with CRS resolution (adjusted $P < 0.05$; Figs. 2E and 3C and Table S17). UFAs exhibit tumor-selective cytotoxicity and provide mitochondrial support for T cells [41,42]. BCAAs contribute to immune modulation, tumor suppression, protein synthesis, and cellular repair [43–45]. Elevated bile acid metabolites were also observed in this trajectory, correlating with liver dysfunction markers (e.g., albumin (ALB), alkaline phosphatase, and gamma-glutamyl transferase (GGT)) and coagulopathy indicators such as platelet count (Fig. S4C and Table S16) [46,47].

Metabolites enriched in glycerophospholipid metabolism in T4, such as lysoPC and acetylcholine, were associated with platelet activation and coagulation (adjusted $P < 0.05$; Figs. 2E and S5B and Tables S16 and S17) [24]. International normalized ratio (INR) and prothrombin time (PT) were negatively correlated with bile acid synthesis markers [48], thereby associating bile acid metabolism with coagulation dysfunction (Figs. S4D, S5A, and S5B) [49]. Increased glycerophospholipid levels were associated with enhanced CAR-T therapy efficacy (Tables S19 and S20), suggesting a role in regulating immune responses. Tryptophan metabolism was also enriched in T4 (Fig. 2E). Indole derivatives were immunomodulatory factors enriched in this pathway, influencing T cell activation and differentiation [50]. Low tryptophan levels were associated with diminished CAR-T cell function, highlighting its importance in metabolic regulation.

The "supraHex" clustering results aligned closely with the "Mfuzz" trajectory analyses, providing comprehensive insights into metabolic changes following CAR-T therapy (Fig. S5C and Table S6) [21]. Pathway enrichment analysis revealed close links among amino acid, lipid, and energy metabolism, and these pathways played important roles in CAR-T therapy responses and associated adverse effects. Correlation results are detailed in the supplementary material.

Differential clinical and metabolic characteristics between severe and mild CRS

As previously described, patients were categorized into two groups: severe and mild CRS groups (Fig. 1A). First, baseline clinical characteristics of the groups were well-balanced. All parameters were similar except for ALT ($P = 0.049$; Table 2). Longitudinal analysis of 66 clinical laboratory characteristics identified six that differed significantly between the groups (Fig. 4A). CysC levels remained elevated above the upper reference limitation in both groups during therapy, but they were higher in the mild group than in the severe group (Fig. 4A). CysC exerts anti-inflammatory effects by inhibiting IL-1β and TNF-α expression without altering IL-6 and IL-8 levels [36]. The inverse relationship between CysC concentration and CRS severity was confirmed in the independent validation cohort (Fig. S15B). GGT and LDH levels in the severe group exceeded those in the mild group at Days 6–9, peaking during the CRS outbreak. LDH levels are correlated with CRS severity in patients with B cell acute lymphoblastic leukemia treated by CAR-T [51]. IL-10 exhibited the largest differences at Days 6–9, peaking before the CRS outbreak (Fig. 4A). Levels were elevated in the severe group, consistent with prior findings linking IL-10 to the severity of CAR-T therapy toxicity (which matched the domain design of our product) [13,52]. After the CRS outbreak, ALT and albumin/globulin ratio (A/G) levels were significantly elevated in the severe group, highlighting heightened liver dysfunction associated with severe CRS [51].

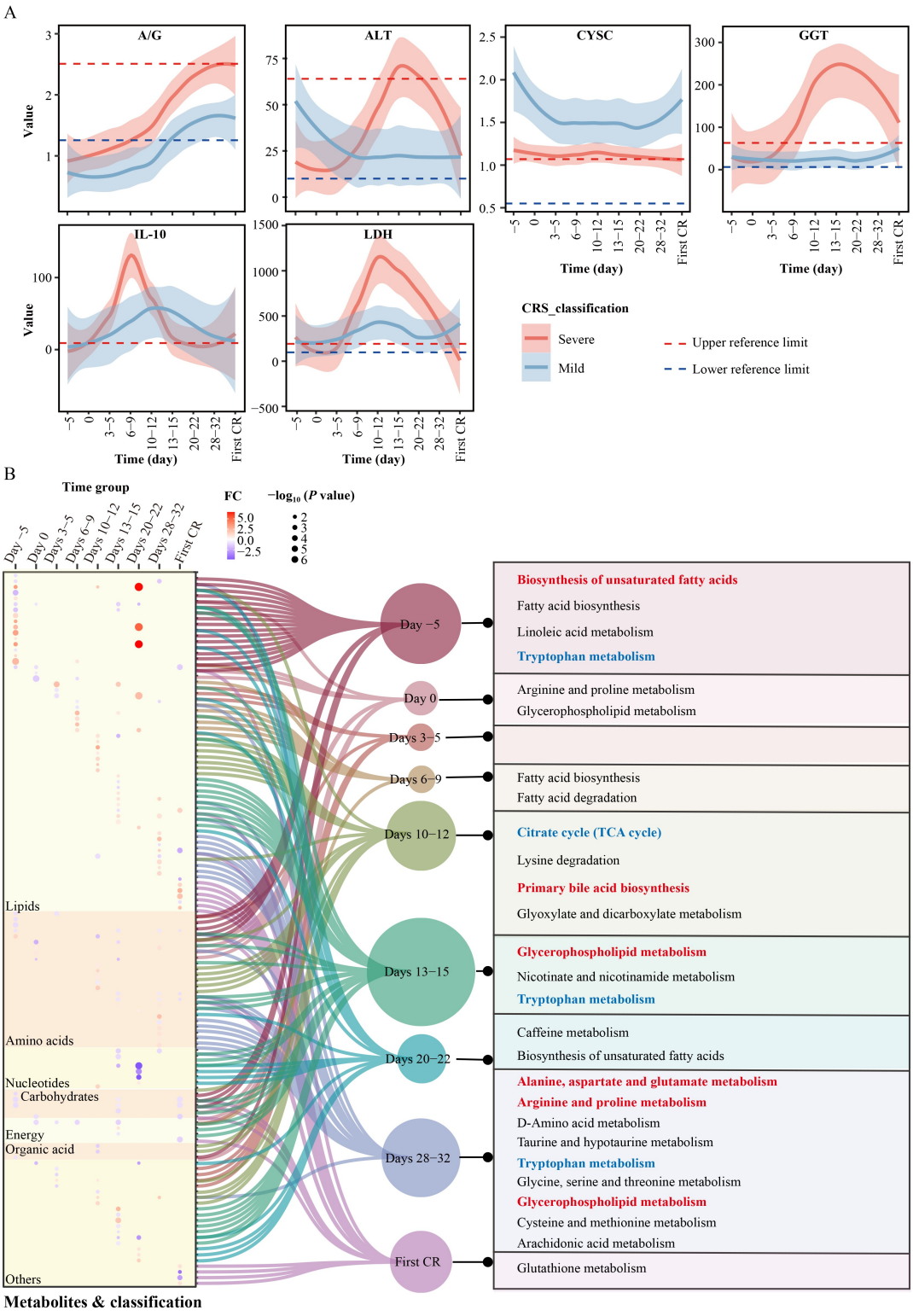

Fig. 4 Dynamic clinical laboratory characteristics and metabolite profile of the severe and mild CRS groups. (A) Differential clinical laboratory characteristics between the severe and mild groups. (B) Differential abundance metabolites between the severe and mild groups in different time points and the enriched KEGG pathways. Left: bubble plot showing the differentially expressed metabolites between the severe and mild groups (FC > 1.5 presents upregulation in the severe group, whereas FC < 0.667 presents downregulation in the severe group). The size of bubbles presents the significance of the difference between the severe and mild groups. Middle: different time slots. The size of circles presents the number of differentially abundant metabolites in each time point. Right: KEGG pathway enrichment in each time group, with annotated metabolites exceeding two within a single pathway. Red indicates upregulation in the severe group, and blue indicates downregulation in the severe group.

Early metabolic shifts (pre-lymphodepletion) as predictors of CRS severity

Lipids and amino acids were the primary metabolites differentiating the severe and mild CRS groups, particularly at three key time slots: Day −5 (pre-lymphodepletion), Days 10–15, and Days 28–32 (Fig. 4B and Table S21). At Day −5, over half of the differential metabolites were significantly enriched in the UFA synthesis pathway, with all involved metabolites significantly upregulated (Fig. 4B (left)). Although UFAs exhibit an established association with obesity [53], no significant difference in BMI was observed between the severe and mild groups in the discovery cohort, suggesting that these metabolic shifts are independent of obesity. These changes likely prepared the immune system by altering cell membrane composition, enhancing immune cell activation, and promoting cytokine release (Figs. 4B (right), S6, and S7 and Table S22) [54]. Additionally, tryptophan metabolism was consistently downregulated in the severe group across multiple time slots, including Day −5, Days 13–15, Days 28–32, and First CR groups. This downregulation of the tryptophan–kynurenine pathway and related metabolites suggested a heightened anti-tumor immune response driven by CAR-T therapy, which may have exacerbated cytokine release and CRS severity (Fig. S8A) [55,56].

Day −5 emerged as a critical time point for predicting CRS. Initial metabolic shifts, particularly in UFA synthesis and tryptophan metabolism, predicted CRS severity. These two pathways highlight systemic immune activation that prepares the immune environment for the onset of CRS. Differences between Days 10–12 and Days 13–15 further emphasize how metabolic pathways shift as CRS progresses, from acute organ damage to inflammatory resolution, highlighting potential opportunities for therapeutic intervention.

Distinct metabolic pathways during CRS development in the severe versus mild groups

During the acute aggravation period (Days 10–15), different metabolic changes were found between the severe and mild CRS groups (Fig. 4B). Primary bile acid synthesis showed a significant increase in the severe group, and these metabolites were strongly associated with coagulation dysfunction markers such as DBIL and FERRIT (Fig. S5B and Table S16). This indicated hepatic impairment and its potential contribution to coagulation dysfunction, possibly due to diminished thrombin production. Additionally, suppression of the TCA cycle was observed (Figs. 4B and S6), indicating decreased mitochondrial energy production. During severe CRS, cells appeared to rely more heavily on glycolysis (instead of TCA) for energy generation. Elevated levels of 5-hydroxylysine (Figs. 4B and S6), a lysine derivative associated with liver fibrosis and tissue damage [57], further emphasized the role of lysine metabolism in the potential long-term organ injury following severe CRS.

On Days 13–15, the middle-to-late phase of CRS outbreak, extensive metabolic differences emerged. Numerous metabolites changed, including those involved in lipid, nucleic acid, carbohydrate, and energy-related metabolites (Fig. 4B, left and middle). Lipid metabolism, particularly glycerophospholipid metabolism, remained prominent, with several metabolites contributing to immune signals and membrane remodeling [58]. Glycerophosphorylcholine is also a key hypertension biomarker [59]; however, PCA of all pre-lymphodepletion metabolites showed that hypertensive status (presence or absence) did not effectively discriminate across patients, excluding hypertension as a primary factor influencing the observed differences. Simultaneously, declining levels of dehydroepiandrosterone and dehydroepiandrosterone sulfate (Fig. S6), known inhibitors of pro-inflammatory cytokine production [58], likely exacerbated cytokine release and amplified inflammatory damage.

Days 28–32 reflected the recovery phase or long-term metabolic changes after CRS, with lipid and amino acid metabolism remaining dominant. Approximately half of the differential metabolites were enriched in glycerophospholipid metabolism, whereas others were involved in phenylalanine, glutamate, and arginine/proline metabolism. Severe CRS cases exhibited elevated glycerophospholipid metabolism, correlating with coagulation dysfunction (Table S16). LysoPC/PE metabolites, choline phosphate, and 4-pyridoxine showed negative correlations with INR, PT, and APTT, emphasizing their role in impaired coagulation pathways (Fig. S5B and Table S16) [60,61].

To further explore metabolite–CRS grade relationships, serum samples were stratified by CRS grade (0–4). Thirty-six metabolites were significantly associated with CRS grades, clustering into four distinct clusters (Fig. S8A and S8B). Metabolites in the top cluster (Fig. S8A), which markedly increased in CRS grade 4, were predominantly associated with primary bile acid synthesis. Notably, all grade 4 samples were collected from the same patient (RJ31), who suffered severe liver damage due to secondary CAR-T re-expansion. Metabolites in this cluster showed a sharp increase in RJ31 on Days 28–32, exceeding levels in all other patients (Fig. S8C).

Severity-dependent temporal metabolic pathways in CRS

The severe and mild groups exhibited distinct metabolic trajectories throughout CAR-T therapy. In the mild group,

metabolites in Trajectory 3 increased after CAR-T infusion, peaking at Days 13–15, whereas those in Trajectory 4 dropped after CAR-T infusion. Metabolites in Trajectory 3 reached their lowest point at Days 20–22 before returning to baseline (Fig. S9), reflecting a gradual and regulated metabolic shift in mild CRS. Conversely, the severe group exhibited an early increase in metabolites in Trajectory 3 (Days 6–9), reaching a peak at Days 10–12, indicating a pronounced metabolic response (Fig. S9). Metabolites in Trajectory 4 decreased after CAR-T infusion but later rebounded beyond baseline levels, indicating sustained metabolic dysregulation.

To elucidate metabolic differences within the severe group, we performed model-based clustering [23] to stratify patients into distinct subgroups. The determination of the optimal number of clusters (G) was guided by stability and validity indices (Fig. 5A and 5B). Evaluation of the stability matrices for G values from 2 to 4 revealed the most consistent consensus at G=2 (Fig. 5A). This finding was corroborated by cluster validity metrics; the functional Davies–Bouldin (fDB) index reached its minimum at G=2 while accounting for sample size constraints, indicating optimal cluster separation and compactness (Fig. 5B). Consequently, we established G=2 as the optimal scale and thereby defined two distinct subgroups: severeA (RJ04, RJ05, RJ26, and RJ29) and severeB (CZ02, CZ03, RJ02, RJ03, RJ22, RJ23, RJ24, RJ25, and RJ27), for subsequent analysis of their metabolic differences (Fig. 5C). The Sankey diagram showed that severeB had higher similarity to the overall severe group than severeA (Fig. 5D), whereas KEGG pathway enrichment revealed that severeA exhibited metabolic profiles more akin to the mild group than severeB (Fig. 5E). This subgrouping approach elucidated metabolic changes in severe CRS, highlighting enhanced energy metabolism (TCA cycle) and amino acid metabolism (e.g., arginine, lysine, and tryptophan metabolism) induced by CAR-T therapy.

Personalized metabolic monitoring: hepatotoxicity in a fatal CRS case (RJ31)

In our previous study, patient RJ31 experienced two severe CRS outbreaks (≥ Grade 3) during CAR-T cell therapy, occurring on Days 6–9 and Days 20–22, respectively [23]. During the first CRS, metabolomics analysis using KEGG enrichment and DA scoring revealed enhanced tryptophan and caffeine metabolism, along with significant suppression of the glycerophospholipid metabolism (Fig. S10A and S10D and Tables S23–S25). After tocilizumab administration, CRS symptoms gradually improved at later time points (Days 10–12 and Days 13–15).

By contrast, the metabolic profile during the second CRS was markedly different (Fig. S10B and S10D and Tables S23–S25). An increase in primary bile acid synthesis, which was previously associated with hepatic impairment (Fig. S5A and Table S16), was consistent with the clinical observation of progressing jaundice. The patient eventually died of liver failure. Additionally, in the second CRS, energy metabolism pathways, such as the TCA cycle and glyoxylate and dicarboxylate metabolism, were significantly activated. Compared with the first CRS, the second CRS episode demonstrated severe liver dysfunction (evident in primary bile acid synthesis) and significant upregulation of energy metabolism (TCA cycle and oxidative phosphorylation) and glycerophospholipid metabolism (Fig. S10C and S10D and Tables S23–S25). These results aligned well with our previously reported PBMC RNA-Seq findings [23].

The death of patient RJ31 after CAR-T therapy may have resulted from serious metabolic problems that established a microenvironment favoring hepatotoxicity. Metabolomic profiling across nine time points showed extreme changes (≥ 5 times the maximum or minimum) in ten key metabolites, namely, N(2)-acetyllysine, 3-dehydroxycarnitine, D-arginine, homoarginine, N-acetylornithine, L-arginine, acetylcholine, Glu-Gln, leukotriene D4 methyl ester, and sulfolithocholylglycine (Fig. 5F and Table S26). Among these, N(2)-acetyllysine consistently exhibited the highest levels, indicating dysregulated lysine acetylation [62], which is an important post-translational modification involved in mitochondrial function [63,64], oxidative phosphorylation [65], and fatty acid metabolism [66]. Excessive lysine acetylation may have impaired mitochondrial function, increased oxidative stress, and weakened antioxidant defenses such as superoxide dismutase (SOD) [63,64]. These metabolic disturbances, along with CRS, resulted in serious liver damage.

In addition to dysregulated lysine acetylation, the biosynthesis of arginine, including L-arginine and N-acetylornithine, increased. Arginine is essential for T cell proliferation and activation [26,27]. In RJ31, this may have facilitated CAR-T cell expansion, intensifying inflammation and worsening CRS severity. Furthermore, metabolites associated with liver injury markers, such as 3-dehydroxycarnitine (linked to glycerophospholipid metabolism and hepatocarcinogenesis) and sulfolithocholylglycine (a bile acid-related hepatotoxicity marker [67]), were modified. Leukotriene D4 methyl ester, a product of AA metabolism, markedly increased, suggesting an overactive inflammatory response that further impaired hepatic function. The metabolic dysregulation in RJ31, characterized by excessive lysine acetylation and heightened arginine biosynthesis, created a microenvironment conducive to CAR-T cell proliferation and systemic inflammation, thereby

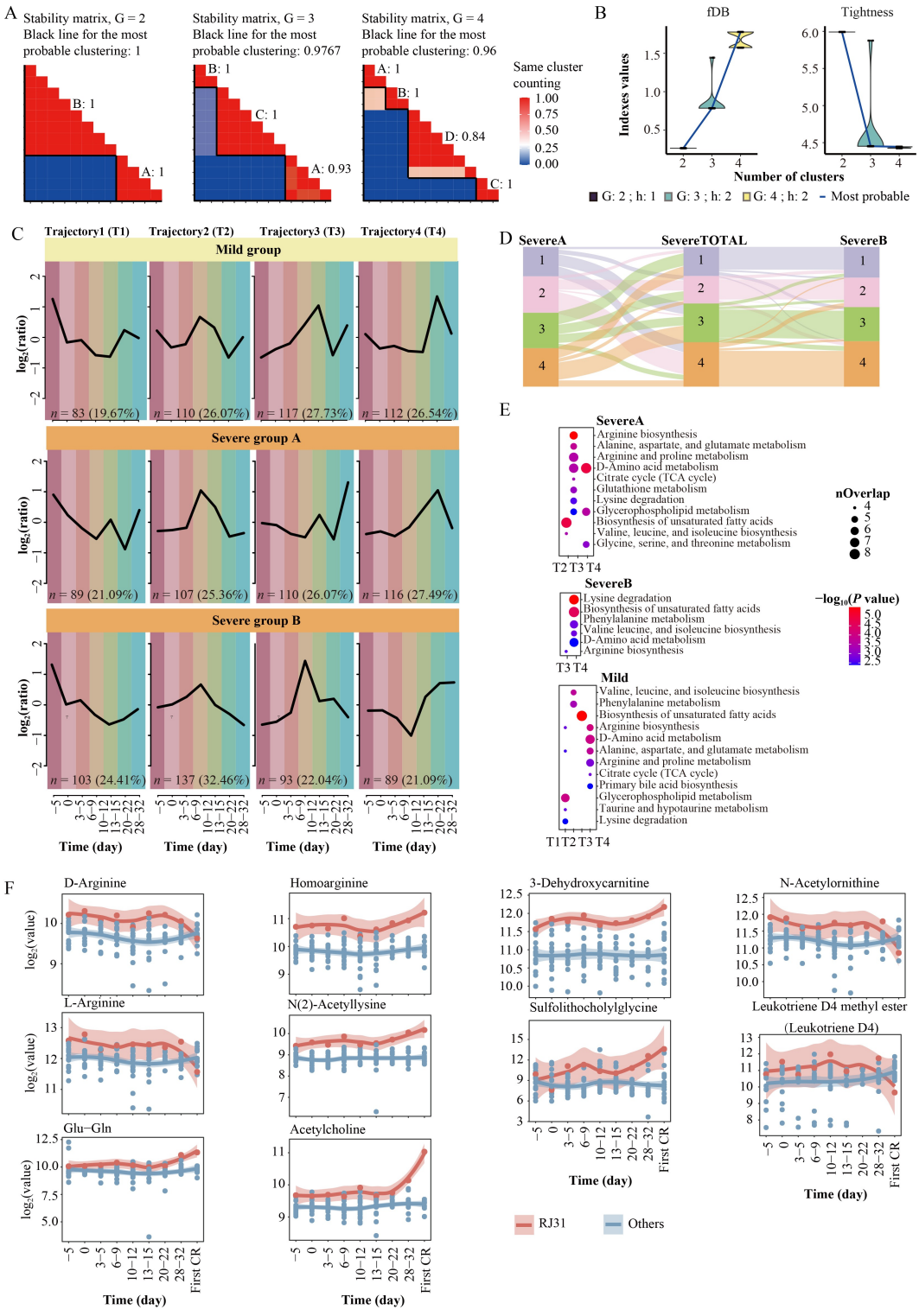

Fig. 5 Dynamic metabolomic profiling between different groups (divided by CONNECTOR) and differential metabolites in RJ31. (A) Stability matrix for parameter G (the number of clusters) = 2, 3, 4, separately. (B) Violin plots depict the distribution of functional Davies–Bouldin (fDB) index values across multiple runs for varying cluster numbers (G) in the left panel, whereas the right panel illustrates the total tightness (T) across different values of G. The optimal clustering scale is determined at G = 2, where the fDB index reaches its minimum while considering sample size constraints. The parameter h, defined as the dimensionality, was optimized automatically by CONNECTOR to ensure robust model estimation. (C) The four different trajectories of metabolites in the severeA, severeB, and mild groups, with differential longitudinal trajectories computed by "Mfuzz" analysis. (D) Sankey plot of metabolites belong to differential trajectories in three groups. (E) Pathway enrichment of the metabolites in four trajectories from three different groups mentioned in Fig. 5C. (F) River plot of differential metabolites.

elevating the risk of severe hepatotoxicity, which was further exacerbated by immune dysfunction. In RJ31, CAR-T clone expansion, HHV7 reactivation, and TET2 mutation elicited a robust inflammatory responses [23]. These metabolic disruptions corresponded with significant immune alterations (as revealed by RNA sequencing and TCR sequencing analyses in our previous work [23]), collectively contributing to fatal liver failure.

Metabolic signatures linking CRS pathophysiology to relapse risk

We integrated metabolomic data with clinical phenotypes, including one-year relapse status, CRS onset time, and CAR-T therapeutic efficacy. Patients were classified into these clinical phenotypes, and differential metabolite analysis was conducted over nine time points in the metabolomic data set. The *P* values of significantly differential metabolites were then used as input for Fisher's combined probability test [68]. Finally, metabolites that significantly influence multiple phenotypes were identified based on the combined *P* value (Fig. S11 and Table S27).

Pathway enrichment analysis revealed that these metabolites are mainly involved in glycerophospholipid metabolism, lysine degradation, phenylalanine metabolism, caffeine metabolism, and glutathione metabolism (Fig. S11 and Table S28). Notably, the glutathione metabolism pathway was not enriched in any analysis, despite glutathione being the most abundant antioxidant in living organisms and crucial for maintaining cellular redox homeostasis [69].

Regression analysis identifies metabolites that predict the timing of CRS onset

To identify prospective serum metabolites associated with the timing of CRS onset, we analyzed relative metabolite abundance at Day −5 and Day 0, classifying expression levels as high or low based on median values. Cumulative incidence analysis revealed 41 metabolites at Day −5 and 46 metabolites at Day 0 that significantly differentiated the timing of CRS onset (Figs. S12 and S13). These metabolites served as input for regression analyses, including lasso, ridge, elastic net, and random forest, to further refine the candidates. Two principal metabolites were identified as being related to the timing of CRS onset (Fig. 6B and Table S29), namely, lysoPC (16:0) and lysoPC (15:0). They functioned as protective factors, with high levels associated with delayed CRS onset (Fig. 6B). Choline phosphate, which reduces inflammation and protects blood vessels [70], was identified via cumulative incidence analysis as a potential protective factor that may delay CRS onset.

Additionally, carnitine has been reported to inhibit cytokine release in certain contexts [71]. The protective effect of the two lysoPC metabolites was also observed in the validation cohort. To address concerns regarding confounding effects of renal impairment on carnitine metabolism [72], we performed a comparative analysis of renal function between CRS severity groups. This demonstrated no significant difference in estimated glomerular filtration rate (mild CRS: 91.3 ± 14.3 vs. severe CRS: 99.5 ± 35.0 mL/min/1.73 m^2, $P = 0.61$), effectively accounting for this comorbidity-related variable. In summary, this metabolome-based regression analysis approach highlights the pivotal role of dysregulated metabolic pathways on the onset and severity of CRS, while also suggesting potential biomarkers for early prediction and therapeutic intervention.

Metabolic differences associated with one-year relapse: protective roles of phosphocholines

Patients were stratified based on their one-year relapse status into two groups (relapsed vs. non-relapsed), for which differential metabolite analysis was performed across all nine time points using the "limma" R package (Fig. S14 and Tables S2 and S30). At Days 20–22, ten metabolites, including sn-glycero-3-phosphocholine, theophylline, taurine, 4-formylindole, and L-dehydroascorbic acid, completely distinguished the relapsed from non-relapsed groups based on Z-scored data. Among these, sn-glycero-3-phosphocholine, a derivative of glycero-3-phosphocholine, typically acts as a protective factor for CRS onset by delaying its occurrence; nevertheless, it was also associated with an increased risk of relapse within 1 year. By contrast, the remaining metabolites reduced relapse risk. For example, a class of choline phosphate metabolites has demonstrated anti-inflammatory properties in various studies. It is widely used as a coating material in coronary artery bypass surgery, significantly reducing the release of pro-inflammatory cytokines and maintaining platelet functionality [71]. Additionally, oxidized choline phosphate exerts anti-inflammatory effects by targeting non-classical macrophage inflammatory vesicles, elevating their activation thresholds, and suppressing inflammation [70].

Independent validation of metabolic biomarkers for CRS severity and onset timing

We established an independent validation cohort comprising 89 samples from 23 patients (Fig. 6A and Table S31) to validate findings from the discovery cohort (117 samples from 19 patients mentioned above). A total of 422 and 473 metabolites were identified in the discovery and validation cohorts, respectively (Tables S6

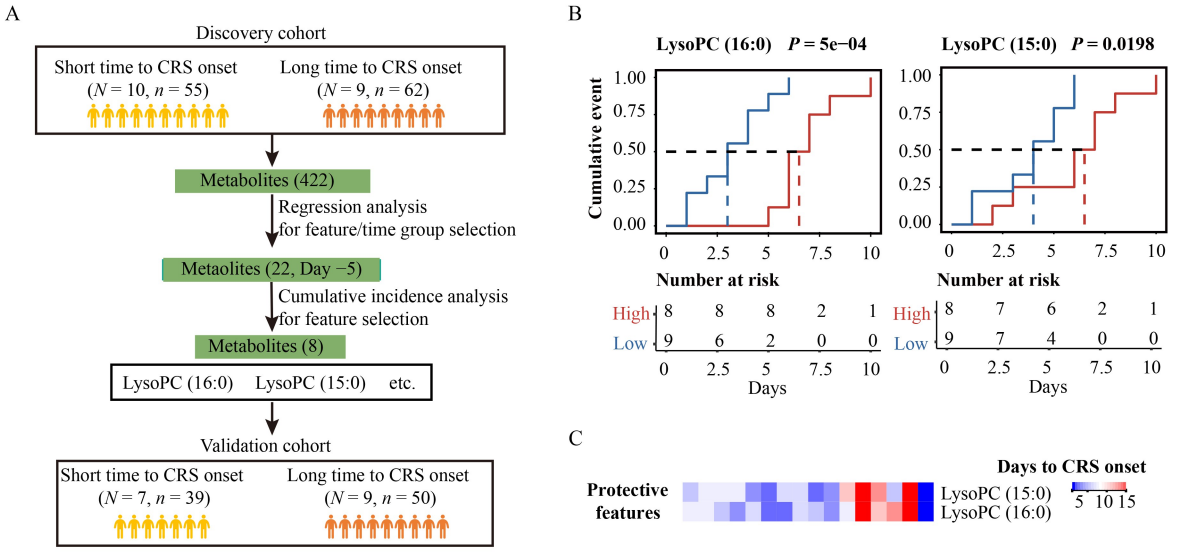

Fig. 6 Metabolites related to CRS onset. (A) Workflow for machine learning in discovery and validation cohorts. "*N*" presents the number of patients; "*n*" presents the number of serum sample. (B) Kaplan–Meier curves for the two metabolites derived from multiple regression analysis, displaying the proportion of patients who experienced CRS, stratified by median metabolite level. (C) Heatmap of the two metabolites in the validation cohort.

and S34), with more lipids detected in the validation cohort than in the discovery cohort. A total of 210 metabolites (including key amino acids) were consistently identified across both data sets (Fig. S15A).

Validation confirmed prior observations: six enriched UFAs maintained their associations with CRS severity, showing a dose-dependent trend with CRS grade (Fig. S16A). This independent replication provides further validation for UFAs as potential biomarkers for stratifying CRS severity. Furthermore, the validation cohort confirmed the inverse relationship between serum tryptophan levels at Day −5 and CRS severity. Given that the tryptophan-kynurenine pathway activity accounts for ~95% of tryptophan metabolic flux, patients with lower kynurenine levels exhibited higher CRS grades (Fig. S16A), strongly supporting its predictive value for severity.

Among the metabolites previously associated with the timing of CRS onset in the discovery cohort, five were identifiable in the validation cohort (Fig. S16B). Notably, the protective role of specific lysoPCs was validated: elevated serum lysoPC (16:0) and lysoPC (15:0) were significantly correlated with delayed CRS onset. Collectively, this independent validation supports the prognostic value of UFAs and kynurenine for stratifying CRS severity, and lysoPCs for predicting delayed CRS onset. In the validation cohort, core metabolic markers showed directional consistency (Fig. 6C), indicating that the revealed immunometabolic mechanisms represent essential CRS pathophysiology rather than construct-specific effects. Although the differences in CAR-T products within cohorts warrant further investigation, our findings lay the groundwork for enhancing CAR-T safety and early application, pending validation in large, multi-product cohorts.

Discussion

In this study, we conducted a comprehensive multi-omics analysis of 19 patients with R/R MM, focusing on metabolomics combined with other multi-omics data. The main feature of this study is the high density of sample collection time points and longitudinal serum metabolic profiling. These approaches systematically revealed the complex relationship between the metabolic dynamic changes during CAR-T therapy and CRS mechanism, offering new perspectives for clinical management.

The dysregulation of arginine metabolism (e.g., *ASS1* upregulation-mediated citrulline depletion) and other metabolic profile features indicate M1 macrophage activation during the fever period (Days 6–9); the significant consumption of citrulline notably precedes the extensive cytokine release, suggesting its crucial role in the early prediction of CRS (Fig. 3) [31,73]. This is consistent with previous research on systemic inflammatory conditions, including sepsis [74], severe COVID-19 [75], and CAR-T-associated CRS [76], which highlight the conserved roles of these metabolites in immune dysregulation. For instance, arginine metabolism dysregulations (e.g., citrulline/aspartate depletion and asymmetric dimethylarginine accumulation) are correlated with endothelial dysfunction and T cell exhaustion in disorders such as sepsis and COVID-19 [74,75]. Similarly, strong correlations between key

arginine metabolites (e.g., citrulline and aspartate) and CRS-related cytokines (e.g., IL-6 and IL-12 p70) have been observed in patients with severe COVID-19 [75]. The imbalance of arginine metabolism not only affects T cell function [25–28], but the overproduction of its derivative nitric oxide (NO) may further damage the vascular endothelium and exacerbate CRS [29]. In addition, significant changes in bile acid metabolism (e.g., elevated sulfolithocholylglycine) are correlated with hepatic injury and coagulation dysfunction, suggesting the need for monitoring hepatic metabolism in CRS management.

The translational potential of our metabolomic discoveries is significantly strengthened by validation in an independent validation cohort (n = 23 patients). First, the association between UFAs and CRS severity, originally observed in the discovery cohort, was replicated (Fig. S16A), confirming UFAs as stratification biomarkers. Second, we validated the inverse correlation between Day −5 serum kynurenine (capturing ~95% of tryptophan flux) and CRS severity grades, reinforcing its role for early risk prediction (Fig. S16A). Mechanistically, this aligns with kynurenine's immunosuppressive properties and UFA-mediated modulation of membrane fluidity and immune cell activation [58]. Third, we validated the protective effect of lysoPC (16:0/15:0) against rapid CRS onset, with high serum levels correlating with delayed onset (Fig. 6B and 6C). Notably, no existing literature links lysoPCs to CRS onset; however, lysoPCs are widely recognized as biomarkers of inflammation and membrane remodeling, consistently decreasing in acute inflammatory states (e.g., sepsis [77] and macrophage polarization [78]) and correlating with disease severity [77], a pattern we also observed in CRS. Our study uniquely identified only these two lysoPC species as offering protection against early CRS onset, providing a physiologic basis for targeting lysophospholipid pathways in early interventions.

The metabolic profile of patient RJ31 (characterized by lysine acetylation hypersynthesis and arginine dysregulation) reveals how metabolic microenvironments influence CAR-T hyperactivation and hepatotoxicity. The metabolic dysregulation in this patient indicates a fatal CRS subtype characterized by liver-specific pathology, resulting from a unique convergence of viral reactivation (HHV7), a rare somatic TET2 mutation, and persistent plasma antigens [23]. This case highlights the importance of a "metabolic–immune–genomic axis" in high-risk CRS, suggesting that such toxicity may be mitigated by early metabolic interventions, particularly given the established role of arginine pathway disruption.

Despite the independent validation of core findings, limitations persist. Our discovery cohort size (N = 19) is limited, and the small sample size of the mild CRS group (N = 4) compromised statistical power for subgroup analyses, particularly for stratified metabolic trajectory comparisons. Furthermore, mechanistic insights from RJ31 require large cohorts. Although the validation cohort confirmed core biomarkers (UFAs, kynurenine, and lysoPCs), some associations showed directional consistency without statistical significance, possibly due to reduced statistical power in subgroups, technical variability across multi-center collection sites, or differential effects of CAR-T product (cilta-cel vs. validation cohort constructs). Notably, correlative findings need functional validation (e.g., use of arginase knockout models). We are organizing follow-up studies to investigate these mechanisms, including assessments of immune cell metabolic shifts, cytokine release dynamics, and inflammasome activation in the presence of lysoPC (16:0/15:0). These experiments will help clarify how these specific lysoPC species influence CRS onset at a molecular level.

In conclusion, this study elucidates the metabolic landscape of CRS and highlights the efficacy of longitudinal multi-omics integration. Independent validation of UFA, tryptophan (via kynurenine), and lysophospholipid biomarkers establishes a clinically actionable framework for predicting CRS severity and kinetics. Implementing these biomarkers may facilitate risk-adaptive prevention (e.g., optimized IL-6R blockade timing), reduce ICU admissions, accelerate CAR-T deployment in previous lines of therapy, and ultimately convert CRS management from reactive intervention to proactive prevention. Although large multi-center studies are necessary, this work lays the foundation for metabolomics-guided risk classification in CAR-T therapy.

Acknowledgements

This work was supported by the State Key Laboratory of Medical Genomics, the Double First-Class Project (No. WF510162602) from the Ministry of Education; Overseas Expertise Introduction Project for Discipline Innovation (111 Project; No. B17029); National Natural Science Foundation of China (Nos. 82230006, 82470206, 32170663, 32470681, and 81770124); Innovative Research Team of High-level Local Universities in Shanghai and CAMS Innovation Fund for Medical Sciences (No. CIFMS 2021-I2M-5-010); Shanghai Municipal Education Commission-Gaofeng Clinical Medicine Grant Support (No. RC20210190).

Compliance with ethics guidelines

Conflicts of interest Xiaolin Ma, Tuantuan Gui, Shuangshuang Yang, Shiwei Jin, Jing Qiao, Yinyin Xie, Junyu Wang, Wanyan Ouyang, Gaoxian Song, Xiao Yi, Chenglin Liu, Mengmeng Pan,

Weiyang Liu, Niu Qiao, Yuting Dai, Yi Tao, Jie Xu, Tong Yin, Hai Fang, and Jianqing Mi declare that they have no conflict of interest. Sai-Juan Chen is the Editor-in-Chief of *Frontiers of Medicine*, who was excluded from the peer-review process and all editorial decisions related to the acceptance and publication of this article. Peer-review was handled independently by the other editors to minimise bias.

The study was approved by the Ruijin Hospital Ethics Committee and the study was performed in accordance with the ethical standards as laid down in the 1964 Declaration of Helsinki and its later amendments or comparable ethical standards. Informed consent was obtained from all patients for being included in the study.

Data availability and compliance statement

The authors declare that the acquisition and subsequent use of all data presented in this manuscript comply fully with all relevant local, national, and international laws, regulations, ethical guidelines (including ClinicalTrials.gov approval numbers NCT03758417 and NCT05759793; Chinese Clinical Trial Registry approval numbers ChiCTR-ONH-17012285 and ChiCTR1900028573; Center for Drug Evaluation (CDE), National Medical Products Administration (NMPA) approval numbers CTR20192510 and CTR20181007), and the terms of use associated with the original data sources.

The authors bear full legal responsibility for ensuring the legality of data acquisition and all subsequent uses.

Electronic supplementary material Supplementary material is available in the online version of this article at https://doi.org/10.1007/s11684-025-1176-9 and is accessible for authorized users

References

1. Rajkumar SV, Dimopoulos MA, Palumbo A, Blade J, Merlini G, Mateos MV, Kumar S, Hillengass J, Kastritis E, Richardson P, Landgren O, Paiva B, Dispenzieri A, Weiss B, LeLeu X, Zweegman S, Lonial S, Rosinol L, Zamagni E, Jagannath S, Sezer O, Kristinsson SY, Caers J, Usmani SZ, Lahuerta JJ, Johnsen HE, Beksac M, Cavo M, Goldschmidt H, Terpos E, Kyle RA, Anderson KC, Durie BGM, Miguel JFS. International Myeloma Working Group updated criteria for the diagnosis of multiple myeloma. Lancet Oncol 2014; 15(12): e538–e548
2. Braggio E, Kortum KM, Stewart AK. SnapShot: multiple myeloma. Cancer Cell 2015; 28(5): 678
3. Kumar SK, Therneau TM, Gertz MA, Lacy MQ, Dispenzieri A, Rajkumar SV, Fonseca R, Witzig TE, Lust JA, Larson DR, Kyle RA, Greipp PR. Clinical course of patients with relapsed multiple myeloma. Mayo Clin Proc 2004; 79(7): 867–874
4. Pinto V, Bergantim R, Caires HR, Seca H, Guimaraes JE, Vasconcelos MH. Multiple myeloma: available therapies and causes of drug resistance. Cancers (Basel) 2020; 12(2): 407
5. June CH, O'Connor RS, Kawalekar OU, Ghassemi S, Milone MC. CAR T cell immunotherapy for human cancer. Science 2018; 359(6382): 1361–1365
6. Brudno JN, Kochenderfer JN. Recent advances in CAR T-cell toxicity: mechanisms, manifestations and management. Blood Rev 2019; 34: 45–55
7. Teachey DT, Lacey SF, Shaw PA, Melenhorst JJ, Maude SL, Frey N, Pequignot E, Gonzalez VE, Chen F, Finklestein J, Barrett DM, Weiss SL, Fitzgerald JC, Berg RA, Aplenc R, Callahan C, Rheingold SR, Zheng Z, Rose-John S, White JC, Nazimuddin F, Wertheim G, Levine BL, June CH, Porter DL, Grupp SA. Identification of predictive biomarkers for cytokine release syndrome after chimeric antigen receptor T-cell therapy for acute lymphoblastic leukemia. Cancer Discov 2016; 6(6): 664–679
8. Norelli M, Camisa B, Barbiera G, Falcone L, Purevdorj A, Genua M, Sanvito F, Ponzoni M, Doglioni C, Cristofori P, Traversari C, Bordignon C, Ciceri F, Ostuni R, Bonini C, Casucci M, Bondanza A. Monocyte-derived IL-1 and IL-6 are differentially required for cytokine-release syndrome and neurotoxicity due to CAR T cells. Nat Med 2018; 24(6): 739–748
9. Giavridis T, van der Stegen SJC, Eyquem J, Hamieh M, Piersigilli A, Sadelain M. CAR T cell–induced cytokine release syndrome is mediated by macrophages and abated by IL-1 blockade. Nat Med 2018; 24(6): 731–738
10. Peng JJ, Wang LM, Li ZY, Ku CL, Ho PC. Metabolic challenges and interventions in CAR T cell therapy. Sci Immunol 2023; 8(82): eabq3016
11. Mi JQ, Zhao W, Jing H, Fu W, Hu J, Chen L, Zhang Y, Yao D, Chen D, Schecter JM, Yang F, Tian X, Sun H, Zhuang SH, Ren J, Fan X, Jin J, Niu T, Chen SJ. Phase II, open-label study of ciltacabtagene autoleucel, an anti–B-cell maturation antigen chimeric antigen receptor–T-cell therapy, in chinese patients with relapsed/refractory multiple myeloma (CARTIFAN-1). J Clin Oncol 2023; 41(6): 1275–1284
12. Xu J, Wang BY, Yu SH, Chen SJ, Yang SS, Liu R, Chen LJ, Hou J, Chen Z, Zhao WH, He AL, Mi JQ, Chen SJ. Long-term remission and survival in patients with relapsed or refractory multiple myeloma after treatment with LCAR-B38M CAR T cells: 5-year follow-up of the LEGEND-2 trial. J Hematol Oncol 2024; 17(1): 23
13. Xu J, Chen LJ, Yang SS, Sun Y, Wu W, Liu YF, Xu J, Zhuang Y,

Zhang W, Weng XQ, Wu J, Wang Y, Wang J, Yan H, Xu WB, Jiang H, Du J, Ding XY, Li B, Li JM, Fu WJ, Zhu J, Zhu L, Chen Z, Fan XF, Hou J, Li JY, Mi JQ, Chen SJ. Exploratory trial of a biepitopic CAR T-targeting B cell maturation antigen in relapsed/refractory multiple myeloma. Proc Natl Acad Sci USA 2019; 116(19): 9543–9551

14. Kumar S, Paiva B, Anderson KC, Durie B, Landgren O, Moreau P, Munshi N, Lonial S, Bladé J, Mateos MV, Dimopoulos M, Kastritis E, Boccadoro M, Orlowski R, Goldschmidt H, Spencer A, Hou J, Chng WJ, Usmani SZ, Zamagni E, Shimizu K, Jagannath S, Johnsen HE, Terpos E, Reiman A, Kyle RA, Sonneveld P, Richardson PG, McCarthy P, Ludwig H, Chen W, Cavo M, Harousseau JL, Lentzsch S, Hillengass J, Palumbo A, Orfao A, Rajkumar SV, Miguel JS, Avet-Loiseau H. International Myeloma Working Group consensus criteria for response and minimal residual disease assessment in multiple myeloma. Lancet Oncol 2016; 17(8): e328–e346
15. Qiao N, Lyu Y, Liu F, Zhang Y, Ma X, Lin X, Wang J, Xie Y, Zhang R, Qiao J, Zhu H, Chen L, Fang H, Yin T, Chen Z, Tian Q, Chen S. Cross-sectional network analysis of plasma proteins/metabolites correlated with pathogenesis and therapeutic response in acute promyelocytic leukemia. Front Med 2024; 18(2): 327–343
16. Shen X, Wu S, Liang L, Chen S, Contrepois K, Zhu ZJ, Snyder M. metID: an R package for automatable compound annotation for LC−MS-based data. Bioinformatics 2022; 38(2): 568–569
17. Fan S, Kind T, Cajka T, Hazen SL, Tang WHW, Kaddurah-Daouk R, Irvin MR, Arnett DK, Barupal DK, Fiehn O. Systematic error removal using random forest for normalizing large-scale untargeted lipidomics data. Anal Chem 2019; 91(5): 3590–3596
18. Ritchie ME, Phipson B, Wu D, Hu Y, Law CW, Shi W, Smyth GK. *limma* powers differential expression analyses for RNA-sequencing and microarray studies. Nucleic Acids Res 2015; 43(7): e47
19. Hakimi AA, Reznik E, Lee CH, Creighton CJ, Brannon AR, Luna A, Aksoy BA, Liu EM, Shen R, Lee W, Chen Y, Stirdivant SM, Russo P, Chen YB, Tickoo SK, Reuter VE, Cheng EH, Sander C, Hsieh JJ. An integrated metabolic atlas of clear cell renal cell carcinoma. Cancer Cell 2016; 29(1): 104–116
20. Lokesh Kumar MF. Mfuzz: a software package for soft clustering of microarray data. Bioinformation 2007; 2(1): 5–7
21. Fang H, Gough J. supraHex: an R/Bioconductor package for tabular omics data analysis using a supra-hexagonal map. Biochem Biophys Res Commun 2014; 443(1): 285–289
22. Gregersen H, Vangsted AJ, Abildgaard N, Andersen NF, Pedersen RS, Frolund UC, Helleberg C, Broch B, Pedersen PT, Gimsing P, Klausen TW. The impact of comorbidity on mortality in multiple myeloma: a Danish nationwide population-based study. Cancer Med 2017; 6(7): 1807–1816
23. Yang S, Xu J, Dai Y, Jin S, Sun Y, Li J, Liu C, Ma X, Chen Z, Chen L, Hou J, Mi JQ, Chen SJ. Neutrophil activation and clonal CAR-T re-expansion underpinning cytokine release syndrome during ciltacabtagene autoleucel therapy in multiple myeloma. Nat Commun 2024; 15(1): 360
24. Ke M, Kang L, Wang L, Yang S, Wang Y, Liu H, Gu C, Huang H, Yang Y. CAR-T therapy alters synthesis of platelet-activating factor in multiple myeloma patients. J Hematol Oncol 2021; 14(1): 90
25. Fultang L, Booth S, Yogev O, Martins da Costa B, Tubb V, Panetti S, Stavrou V, Scarpa U, Jankevics A, Lloyd G, Southam A, Lee SP, Dunn WB, Chesler L, Mussai F, De Santo C. Metabolic engineering against the arginine microenvironment enhances CAR-T cell proliferation and therapeutic activity. immunobiology and immunotherapy 2020; 136(10): 1155–1160
26. Liu Y, An L, Huang R, Xiong J, Yang H, Wang X, Zhang X. Strategies to enhance CAR-T persistence. Biomark Res 2022; 10(1): 86
27. Geiger R, Rieckmann JC, Wolf T, Basso C, Feng Y, Fuhrer T, Kogadeeva M, Picotti P, Meissner F, Mann M, Zamboni N, Sallusto F, Lanzavecchia A. L-arginine modulates T cell metabolism and enhances survival and anti-tumor activity. Cell 2016; 167(3): 829–842.e13
28. Martí I Líndez AA, Reith W. Arginine-dependent immune responses. Cell Mol Life Sci 2021; 78(13): 5303–5324
29. George JA, Gounden V. Novel glomerular filtration markers. Adv Clin Chem 2019; 88: 91–119
30. Ji L, Zhao X, Zhang B, Kang L, Song W, Zhao B, Xie W, Chen L, Hu X. Slc6a8-mediated creatine uptake and accumulation reprogram macrophage polarization via regulating cytokine responses. Immunity 2019; 51(2): 272–284.e7
31. Mao Y, Shi D, Li G, Jiang P. Citrulline depletion by ASS1 is required for proinflammatory macrophage activation and immune responses. Mol Cell 2022; 82(3): 527–541.e7
32. Liu Y, Fang Y, Chen X, Wang Z, Liang X, Zhang T, Liu M, Zhou N, Lv J, Tang K, Xie J, Gao Y, Cheng F, Zhou Y, Zhang Z, Hu Y, Zhang X, Gao Q, Zhang Y, Huang B. Gasdermin E–mediated target cell pyroptosis by CAR-T cells triggers cytokine release syndrome. Sci Immunol 2020; 5(43): eaax7969
33. Ricote M, Garcia-Tunon I, Bethencourt FR, Fraile B, Paniagua R, Royuela M. Interleukin-1 (IL-1alpha and IL-1beta) and its receptors (IL-1RI, IL-1RII, and IL-1Ra) in prostate carcinoma. Cancer 2004; 100(7): 1388–1396
34. Nanjireddy PM, Olejniczak SH, Buxbaum NP. Targeting of chimeric antigen receptor T cell metabolism to improve therapeutic outcomes. Front Immunol 2023; 14: 1121565
35. Lakhani A, Chen X, Chen LC, Khericha M, Chen YY, Park JO. Extracellular domains of CARs reprogramme T cell metabolism without antigen stimulation. Nat Metab 2024; 6(6): 1143–1160
36. Gren ST, Janciauskiene S, Sandeep S, Jonigk D, Kvist PH, Gerwien JG, Hakansson K, Grip O. The protease inhibitor cystatin C down-regulates the release of IL-β and TNF-α in lipopolysaccharide activated monocytes. J Leukoc Biol 2016; 100(4): 811–822
37. Robinson AM, Gondalia SV, Karpe AV, Eri R, Beale DJ, Morrison PD, Palombo EA, Nurgali K. Fecal microbiota and metabolome in a mouse model of spontaneous chronic colitis: relevance to human inflammatory bowel disease. Inflamm Bowel Dis 2016; 22(12): 2767–2787
38. Tahtinen S, Tong AJ, Himmels P, Oh J, Paler-Martinez A, Kim L, Wichner S, Oei Y, McCarron MJ, Freund EC, Amir ZA, de la Cruz CC, Haley B, Blanchette C, Schartner JM, Ye W, Yadav M, Sahin U, Delamarre L, Mellman I. IL-1 and IL-1ra are key regulators of the inflammatory response to RNA vaccines. Nat Immunol 2022; 23(4): 532–542
39. Raposa EB, Bower JE, Hammen CL, Najman JM, Brennan PA. A developmental pathway from early life stress to inflammation: the

role of negative health behaviors. Psychol Sci 2014; 25(6): 1268–1274
40. Valinluck V, Sowers LC. Inflammation-mediated cytosine damage: a mechanistic link between inflammation and the epigenetic alterations in human cancers. Cancer Res 2007; 67(12): 5583–5586
41. Nava Lauson CB, Tiberti S, Corsetto PA, Conte F, Tyagi P, Machwirth M, Ebert S, Loffreda A, Scheller L, Sheta D, Mokhtari Z, Peters T, Raman AT, Greco F, Rizzo AM, Beilhack A, Signore G, Tumino N, Vacca P, McDonnell LA, Raimondi A, Greenberg PD, Huppa JB, Cardaci S, Caruana I, Rodighiero S, Nezi L, Manzo T. Linoleic acid potentiates $CD8^+$ T cell metabolic fitness and antitumor immunity. Cell Metab 2023; 35(4): 633–650.e9
42. Das UN. Can bioactive lipids augment anti-cancer action of immunotherapy and prevent cytokine storm? Arch Med Res 2019; 50(6): 342–349
43. Yahsi B, Gunaydin G. Immunometabolism—the role of branched-chain amino acids. Front Immunol 2022; 13: 886822
44. Kates MS, Saibil SD. Reprogramming T cell metabolism to enhance adoptive cell therapies. Int Immunol 2024; 36(6): 261–278
45. Wetzel TJ, Erfan SC, Ananieva EA. The emerging role of the branched chain aminotransferases, BCATc and BCATm, for anti-tumor T-cell immunity. Immunometabolism (Cobham) 2023; 5(1): e00014
46. Han YJ, Hu SQ, Zhu JH, Cai X, Lai DM, Chen BH, Zhu K, Tong Q, Zhou XR, Deng JL, Tou JF, Fang Z, Du LZ. Accurate prediction of biliary atresia with an integrated model using MMP-7 levels and bile acids. World J Pediatr 2024; 20(8): 822–833
47. Ma Q, Liao X, Shao C, Lin Y, Wu T, Sun Y, Feng ST, Ye J, Zhong B. Normalization of gamma-glutamyl transferase levels is associated with better metabolic control in individuals with nonalcoholic fatty liver disease. BMC Gastroenterol 2021; 21(1): 215
48. Jiskani A, Memon S, Naseem L. Prothrombin time (PT), activated partial thromboplastin time (APTT) and international normalized ratio (INR) as predictive factors of coagulopathy in newly diagnosed hypertensive patients. Hematol Transfus Int J 2017; 4(3): 84–88
49. Yan P, Wan Q, Zhang Z, Tang Q, Wu Y, Xu Y, Miao Y, Zhao H, Liu R. Decreased physiological serum total bile acid concentrations in patients with type 2 diabetic peripheral neuropathy. Diabetes Metab Syndr Obes 2021; 14: 2883–2892
50. Panetti S, McJannett N, Fultang L, Booth S, Gneo L, Scarpa U, Smith C, Vardon A, Vettore L, Whalley C, Pan Y, Varnai C, Endou H, Barlow J, Tennant D, Beggs A, Mussai F, De Santo C. Engineering amino acid uptake or catabolism promotes CAR T-cell adaption to the tumor environment. Blood Adv 2023; 7(9): 1754–1761
51. Wei Z, Xu J, Zhao C, Zhang M, Xu N, Kang L, Lou X, Yu L, Feng W. Prediction of severe CRS and determination of biomarkers in B cell-acute lymphoblastic leukemia treated with CAR-T cells. Front Immunol 2023; 14: 1273507
52. Tedesco VE, Mohan C. Biomarkers for predicting cytokine release syndrome following CD19-targeted CAR T cell therapy. J Immunol 2021; 206(7): 1561–1568
53. Li Y, Wang X, Zhang Z, Shi L, Cheng L, Zhang X. Effect of the gut microbiome, plasma metabolome, peripheral cells, and inflammatory cytokines on obesity: a bidirectional two-sample Mendelian randomization study and mediation analysis. Front Immunol 2024; 15: 1348347
54. Stulnig TM, Zeyda M. Immunomodulation by polyunsaturated fatty acids: impact on T-cell signaling. Lipids 2004; 39(12): 1171–1175
55. Ray A, Song Y, Du T, Tai YT, Chauhan D, Anderson KC. Targeting tryptophan catabolic kynurenine pathway enhances antitumor immunity and cytotoxicity in multiple myeloma. Leukemia 2020; 34(2): 567–577
56. Yang L, Chu Z, Liu M, Zou Q, Li J, Liu Q, Wang Y, Wang T, Xiang J, Wang B. Amino acid metabolism in immune cells: essential regulators of the effector functions, and promising opportunities to enhance cancer immunotherapy. J Hematol Oncol 2023; 16(1): 59
57. Wesolowski SR, Mulligan CM, Janssen RC, Baker PR II, Bergman BC, D'Alessandro A, Nemkov T, Maclean KN, Jiang H, Dean TA, Takahashi DL, Kievit P, McCurdy CE, Aagaard KM, Friedman JE. Switching obese mothers to a healthy diet improves fetal hypoxemia, hepatic metabolites, and lipotoxicity in non-human primates. Mol Metab 2018; 18: 25–41
58. Powell JM, Sonnenfeld G. The effects of dehydroepiandrosterone (DHEA) on in vitro spleen cell proliferation and cytokine production. J Interferon Cytokine Res 2006; 26(1): 34–39
59. Sekaran K, Zayed H. Identification of novel hypertension biomarkers using explainable AI and metabolomics. Metabolomics 2024; 20(6): 124
60. Addi T, Dou L, Burtey S. Tryptophan-derived uremic toxins and thrombosis in chronic kidney disease. Toxins (Basel) 2018; 10(10): 412
61. Boyd A, Boccara F, Meynard JL, Ichou F, Bastard JP, Fellahi S, Samri A, Sauce D, Haddour N, Autran B, Cohen A, Girard PM, Capeau J. Serum tryptophan-derived quinolinate and indole-3-acetate are associated with carotid intima-media thickness and its evolution in HIV-infected treated adults. Open Forum Infect Dis 2019; ofz516
62. Guo L, Zhou SR, Wei XB, Liu Y, Chang XX, Liu Y, Ge X, Dou X, Huang HY, Qian SW, Li X, Lei QY, Gao X, Tang QQ. Acetylation of mitochondrial trifunctional protein α-subunit enhances its stability to promote fatty acid oxidation and is decreased in nonalcoholic fatty liver disease. Mol Cell Biol 2016; 36(20): 2553–2567
63. Ali I, Conrad RJ, Verdin E, Ott M. Lysine acetylation goes global: from epigenetics to metabolism and therapeutics. Chem Rev 2018; 118(3): 1216–1252
64. Assiri MA, Roy SR, Harris PS, Ali H, Liang Y, Shearn CT, Orlicky DJ, Roede JR, Hirschey MD, Backos DS, Fritz KS. Chronic ethanol metabolism inhibits hepatic mitochondrial superoxide dismutase via lysine acetylation. Alcohol Clin Exp Res 2017; 41(10): 1705–1714
65. Le-tian Z, Cheng-zhang H, Xuan Z, Zhang Q, Zhen-gui Y, Qing-qing W, Sheng-xuan W, Zhong-jin X, Ran-ran L, Ting-jun L, Zhong-qu S, Zhong-hua W, Ke-rong S. Protein acetylation in mitochondria plays critical functions in the pathogenesis of fatty liver disease. BMC Genomics 2020; 21(1): 435
66. Zhang Y, Ding N, Cao Y, Zhu Z, Gao P. Differential diagnosis between hepatocellular carcinoma and cirrhosis by serum amino acids and acylcarnitines. Int J Clin Exp Pathol 2018; 11(3): 1763–1769

67. Marks JW, Sue SO, Pearlman BJ, Bonorris GG, Varady P, Lachin JM, Schoenfield LJ. Sulfation of lithocholate as a possible modifier of chenodeoxycholic acid-induced elevations of serum transaminase in patients with gallstones. J Clin Invest 1981; 68(5): 1190–1196
68. Fang H, Gough J. The 'dnet' approach promotes emerging research on cancer patient survival. Genome Med 2014; 6(8): 64
69. Bansal A, Simon MC. Glutathione metabolism in cancer progression and treatment resistance. J Cell Biol 2018; 217(7): 2291–2298
70. Chu LH, Indramohan M, Ratsimandresey RA, Gangopadhyay A, Morris EP, Monack DM, Dorfleutner A, Stehlik C. The oxidized phospholipid oxPAPC protects from septic shock by targeting the non-canonical inflammasome in macrophages. Nat Commun 2018; 9(1): 996
71. Schulze CJ, Han L, Ghorpade N, Etches WS, Stang L, Koshal A, Wang SH. Phosphorylcholine-coated circuits improve preservation of platelet count and reduce expression of proinflammatory cytokines in CABG: a prospective randomized trial. J Card Surg 2009; 24(4): 363–368
72. Grams ME, Tin A, Rebholz CM, Shafi T, Kottgen A, Perrone RD, Sarnak MJ, Inker LA, Levey AS, Coresh J. Metabolomic alterations associated with cause of CKD. Clin J Am Soc Nephrol 2017; 12(11): 1787–1794
73. Biswas Subhra K, Mantovani A. Orchestration of metabolism by macrophages. Cell Metab 2012; 15(4): 432–437
74. Guo C, Xie S, Chi Z, Zhang J, Liu Y, Zhang L, Zheng M, Zhang X, Xia D, Ke Y, Lu L, Wang D. Bile acids control inflammation and metabolic disorder through inhibition of NLRP3 inflammasome. Immunity 2016; 45(4): 802–816
75. Xiao N, Nie M, Pang H, Wang B, Hu J, Meng X, Li K, Ran X, Long Q, Deng H, Chen N, Li S, Tang N, Huang A, Hu Z. Integrated cytokine and metabolite analysis reveals immunometabolic reprogramming in COVID-19 patients with therapeutic implications. Nat Commun 2021; 12(1): 1618
76. Arifuzzaman M, Collins N, Guo CJ, Artis D. Nutritional regulation of microbiota-derived metabolites: Implications for immunity and inflammation. Immunity 2024; 57(1): 14–27
77. Arnhold J. Host-derived cytotoxic agents in chronic inflammation and disease progression. Int J Mol Sci 2023; 24(3): 3016
78. Qin X, Qiu C, Zhao L. Lysophosphatidylcholine perpetuates macrophage polarization toward classically activated phenotype in inflammation. Cell Immunol 2014; 289(1–2): 185–190